Journal of Quantitative Spectroscopy & Radiative Transfer 311 (2023) 108773

Contents lists available at ScienceDirect

Journal of Quantitative Spectroscopy and Radiative Transfer

journal homepage: www.elsevier.com/locate/jqsrt

An overview of the optical characterization of free microparticles and their radiative properties

Marco A.C. Potenza *, Llorenç Cremonesi

Department of Physics and CIMAINA, Università degli Studi di Milano, Via Celoria, 16 I-20133, Milano, Italy

ARTICLE INFO

Keywords:
Light scattering
Light extinction
Microparticle optical properties
Aerosol optical properties

ABSTRACT

We discuss how the range of information available from microparticle analysis can be extended in a number of applications by measuring a specific set of optical properties of individual particles using light scattering. Central to these measurements are the real and imaginary components of the forward scattered field, the former being equal to the extinction cross-section except for a few particle-independent constants. Although still a niche technique, it has some inherent advantages and great potential for particle characterization, especially in the challenging near-wavelength size range. A selection of cases is covered from an experimental point of view, while some essential models are introduced to illustrate the underlying physical phenomena. We present a benchmark of experimental results from the literature and other examples that support optical diagnostics applied in science and industrial processes. As a key point of this work, we show that by accessing the fundamental properties of scatterers the inversion of light scattering data can be avoided. This provides model-independent results closer to application requirements without the drawbacks of case-specific assumptions.

1. Introduction

Light scattering is a fundamental and ubiquitous physical process that underlies a wide range of phenomena, from the color of the sky to more complex systems in astronomy or the mechanisms that regulate climate. Similarly, it is used in industry, medical diagnostics, control systems in manufacturing, environmental monitoring, and remote sensing [1,19,51,80,81,143,153,187,210,219]. Irrespective of the specific application, light scattering methods rely on measuring and calculating the fields radiated by given objects: their viability also depends on the capability of solving the *inverse problem*, to retrieve the particle characteristics based on radiative data. Due to the number of possible parameters affecting the radiative properties of even a single particle, this task is impossible without independent experimental information. Advances in theoretical and numerical methods, as well as in computing power, have led to remarkable improvements in this field [143,233,236].

In many cases, scattering properties are the starting point for further analyses based upon, for example, radiative transfer models (RTMs) [24,56,117,133,135,192] with many scientific, technological, and social implications. RTMs need to be fed with specific optical parameters, which may require rough assumptions or imply model-dependent results if not based on solid experimental measurements [2,135,187,195]. Recent directives addressing climate change urge us to deepen our knowledge about light scattering and the working principles of the Earth's energy balance. For example, the 13th Goal of the United Nations 2030 Agenda ("Climate actions"), sets out two fundamental guidelines to reduce and possibly prevent the consequences of climate change: *mitigation and adaptation*. As widely discussed in the Intergovernmental Panel on Climate Change (IPCC) 2021 Report [65], the aerosol contribution is one of its least understood agents. From an alternative perspective, the possibility of developing rapid and non-invasive characterization methods for free nano- and microparticles is attracting the attention of the industry for process optimization and innovative product design (including nanoelectronics, food, and design), as well as for a sound assessment of the functionality, hazards, degradation and environmental impact of engineered particles [107,151,181,188].

In this review, we summarize the main radiative parameters that can be measured with reasonable ease for each particle and from which the most information can be extracted to characterize their physical properties. While the radiative properties of a particle can be outlined in broad strokes by its extinction cross-section, we show that characterizing the forward scattering and the optical thickness is relevant for a variety of applications and is possible on an experimental basis. These

* Corresponding author.
E-mail address: marco.potenza@unimi.it (M.A.C. Potenza).

https://doi.org/10.1016/j.jqsrt.2023.108773
Received 21 February 2022; Received in revised form 7 September 2023; Accepted 9 September 2023
Available online 10 September 2023

parameters are also related to some interesting phenomena that underlie general issues in light scattering. We discuss the physical origin of sizing problems through the study of internal fields. After a brief historical overview, we discuss their role and introduce the intermediate size range as a function of the parameters involved in determining the internal fields of the particle. We outline the connections between these and the homologous scattering diagrams [219], Sorensen's Q-space analysis [202], and the low-angle scattering analysis methods [62] typical of light scattering and X-ray scattering. In Section 3 we summarize the limitations of light scattering approaches that are based on the measurement of just one parameter, with an eye on characterizing single particles beyond their size. The advantages of measuring the real and imaginary components of the forward-scattered field are introduced in Section 4, whereas some experimental methods to characterize this quantity are discussed in Section 5. A benchmark of experimental results is discussed in Sections 6, 7, and 8, where we report some of our formerly published data obtained with a suite of instruments to measure the forward scattering light in both liquid- and air-borne microparticles. Insights are given into the potential applications arising by measuring the forward-scattered field in a widespread class of scientific and technological applications.

1.1. Historical background

Since the studies of precursors like Bruke, Faraday, and Tyndall, it became clear that quantitative explanations demanded robust theoretical descriptions of light scattering, starting from the link between laboratory results and the color of the sky [218]. Just a couple of years after Tyndall's work, Rayleigh introduced his famous model and explained the color of the sky in terms of its microscopic properties: the radiation wavelength and the particle polarizability [184,185]. Rayleigh's assumption of independent scatterers does not quite apply to air molecules and was strongly questioned by Mandel'stam, giving rise to a dispute about the discrete or continuum nature of fluids [126]. Mandel'stam's concern about closely spaced scatterers—with distances much smaller than the wavelength—was correct: the Ewald–Oseen theorem was proved in 1915 [21,203], elucidating the microscopic origin of the refractive index. The transmitted and scattered waves in a bulk medium superimpose giving rise to a slower wave traveling at the speed of light in the medium. The works by Smoluchowski and Einstein just a few years before [55,199] interpreted light scattering as due to density fluctuations in a continuum rather than scatterers, proving the equivalence of the two descriptions (proof of which can be found in the work by Landau [115], §120). Interestingly, inverting the scattering problem for light travelling through pure air is a way to measure Avogadro's Number from the very clear sky [55,163,170,219]. As a matter of fact, sky light is mostly produced by Tyndall's light radiated by independent scatterers composed of eolian dust and aerosols, both natural and anthropogenic, especially in urbanized and polluted regions. The inhomogeneities in the medium are corpuscles of different materials radiating blue light as Tyndall argued for liquid suspensions. We can consider particles as Rayleigh scatterers while their size a is much smaller than the wavelength, say $a < \lambda/20$ [219]: dipoles oscillate in phase (uniform polarization), their radiated fields sum up in phase and the radiated power scales as the squared number of dipoles, hence as a^6. If many scatterers are independent of one another, the radiation from a collection of particles adds up incoherently: the total intensity scales linearly with the number of particles. The polarization of sky light is also a consequence of Rayleigh, or Tyndall, scattering.

Things become much harder to parse when size increases to the wavelength scale, in the so-called *intermediate size range*. Roughly speaking, this occurs in between the Rayleigh ($a \ll \lambda$) and the diffraction (or geometric optics) ($a \gg \lambda$) regimes (see Section 2 for details). In the second half of the nineteenth century, after the major advances made by Young and Fresnel, great mathematical physicists tackled many problems in optics, including light scattering: among others, Poisson, Stokes, Cauchy, Kirchhoff, and Debye [219]. Still, almost none of the major optical problems were solved, scattering from a sphere being one of the hardest, and it was impossible to interpret scattering data. The exact solution was given years later by Ludvig Lorenz and Gustav Mie in 1908 [39,136]. They provided the analytical expressions for the internal and external vector fields and the radiated intensity as a function of the scattering angle in terms of the dimensionless sphere radius, $x = ka$ (the *size parameter)*, and the refractive index of the sphere relative to the surrounding medium, m. Later steps in dealing with light scattering were due to astronomy and continue to this day, with decadal efforts to explain a huge amount of experimental/observational data: reddening of starlight, interplanetary dust, zodiacal light and comet tails, and extinction spectra, to cite a few [48,138,157,219,235]. Some applications to atmospheric optics followed, for example, to measure haze (extinction) and sun haloes (scattering patterns) in the atmosphere [18], as well as atmospheric phenomena on other planets, with the pioneering work by Hansen and Cheyney [79] and recently extended to exoplanets by the James Webb Space Telescope [69]. Towards the end of the twentieth century, the problem of non-spherical, non-homogeneous particles was extensively approached, first in astronomy, then to interpret data from the laser detection and ranging (LIDAR) technique, currently one of the most versatile methods for remote sensing [20,70,89,139]. Inverting data from direct Sun irradiance (extinction) and sky radiance measurements (scattering) opened new perspectives in characterizing aerosols through passive remote sensing, retrieving the optical properties of non-spherical dust [51–53,153,234]. Furthermore, numerical algorithms based on different theoretical approaches have been developed for the quantification of scattering from particles endowed with almost any possible feature, even collections of particles [19,50,53,201].

Lasers have paved the way for new experimental methods, providing unprecedented data and links between theory and observation. Such methods can take advantage of the monochromaticity, sharply focused power, and (in some cases of interest) spatial coherence of laser light [17,93,223]. Many instruments based on the controlled illumination of a sample for scientific and industrial applications, environmental monitoring, and remote sensing have been developed and validated. Since data interpretation aims at differentiating particles based on their scattering features, manageable solutions to the inverse scattering problem and computing methods are required [104]. The differential or total cross-sections, and in some cases the scattering matrix elements, are typically used for this purpose [130,150,190].

1.2. Light scattering methods

Light scattering measurements for characterizing nano- and microparticles usually access one among two complementary observables: i) the intensity of light diffused over a range of angles, possibly including backscattering, or ii) light extinction through a sample [219]. Considerable advances have been achieved in developing methods based on these measurements, overcoming some experimental and metrological shortcomings whose description is beyond the scope of this work [22,27,32,77,130,239,240].

Both scattering and extinction can be measured either from a collection of many particles or one single particle. Decades of development of small-angle light scattering (SALS), multi-angle light scattering (MALS), Dynamic Light Scattering (DLS), and multi-wavelength or spectroscopic extinction measurements have yielded robust and reliable methods for characterizing ensembles of particles: supported or non supported, liquid- or gas- suspended, contained in huge or tiny volumes, carefully stabilized within the container or fast flowing through the scattering region [16,36,44,54,60,91,116,158]. Some recent studies have adopted convolutional neural networks to assess the most significant angle to discriminate single particles from light scattering or characterizing colloidal particle suspensions from their speckle patterns [98,166,167]. Combinations of SALS, MALS, and DLS have been also

adopted [58,120,121,134]. Light scattering methods have been extensively applied to study the kinetics of colloidal aggregation processes [62,131,180,220,228].

When many particles scatter simultaneously, they generate relatively strong signals and facilitate measuring several parameters at a time. On the other hand, the superposition of many contributions makes the properties of the particles mistakable (e.g. size distribution). Inversion involves ill-posed problems, typically hampered by noise and demanding *a priori* assumptions about the solution [217]. Inverting signals is harder as the non-spherical shape increases the number of parameters [20,28,30,222]. Common inversion approaches are adopted for SALS (see for example Ferri et al. [63] and references therein) or DLS [16,66,216]. Huge efforts have provided effective methods to invert data from sunlight irradiance (extinction), sky radiometry (scattering), and LIDAR (backscattering) thanks to extended collaborations worldwide (see for example Dubovik et al. and Nakajima et al. [51,153] and references therein). Nowadays, all these methods are capable of characterizing aerosol particles from kilometers away [23,148]. It is worth mentioning the case of backscattering: it is more sensitive to the size, shape, and internal inhomogeneities of the particles than forward or angular scattering [118,159,224]. When exploited to measure the Mueller matrix elements by collecting light with multipixel sensors, backscattering shows its superior potential in particle characterization [67,118]. A promising alternative for all scattering methods is to exploit data without any inversion: turbidimetry, nephelometry, and ceilometry are examples where concentration, extinction, scattering, backscattering, or total scattering cross-sections of the whole collection of particles illuminated by a known light source are obtained, with the advantage of preserving the model independence of the results [3,4,11,85,152]. As a closing remark to this section, we should also mention light polarization, or rather, the depolarization ratio, as a significant optical parameter extensively studied in literature [130,149], although it is beyond the scope of the present work.

1.3. Optical particle sizing

A general rule dominates scattering measurements, with and without lasers: scattering and extinction cross-sections, as well as the angular dependence of intensity, mainly depend on particle size. Particle shape, orientation, and internal inhomogeneities play a comparatively smaller role and are not usually as accessible [219]. In fact, scattering measurements provide size as the most relevant parameter in most applications, from science to industrial process control [43,95–97,125,187]. On the other hand, one could argue that some parameters — cross-section and size in this case — are related by such fundamental physical laws that measuring the size is more a side effect than a choice. However, *size* is not uniquely defined in all the cases where particles are characterized by different length scales or asymmetries along different axes. As a result, sizing depends on which parameter is measured, as exemplified by comparing results from different methods [35,172,198]. Certified methods for industrial applications are subject to these issues as well, although this is not usually considered in their respective fields of use [95–97].

2. The intermediate size range

The Lorentz–Lorenz formula[1] expresses polarizability in terms of the volume of the particle v and its complex refractive index m relative to the surrounding medium:

$$\alpha = \frac{3v}{4\pi}\frac{m^2-1}{m^2+2} = a^3\frac{m^2-1}{m^2+2} \tag{1}$$

where a is defined as the volume-equivalent radius of the particle [219]. In the following, we will refer to dimensionless quantities, such as the complex scattering amplitude $S(\vartheta)$ and the fluence of the scattered radiation $F(\vartheta) = |S(\vartheta)|^2$ [19,219], with ϑ the angle formed between the incoming and scattered wave directions.

Moving from very small Rayleigh scatterers to the wavelength scale and beyond, the condition of uniform polarization within the particle volume is no longer satisfied. The oscillations of the internal dipoles forced from the incoming wave are not synchronous, disrupting isotropy and coherence in the radiated fields [35]. Between the Rayleigh regime ($a \ll \lambda$) and the diffraction regime ($a \gg \lambda$) (also named geometrical optics regime), interference between the fields radiated by dipole elements within the particle makes the scattered intensity dependent on the particle size, shape, orientation, and observation direction. Additionally, diffraction from the borders forms a new wavefront in the far field of the scatterer (Fraunhofer region) from the superposition of the Huygens–Fresnel–Kirkhoff elementary waves originated by the incomplete wavefront emerging after the scatterer.

In this context, it is convenient to introduce the phase shift parameter, $\rho = 2ka(m-1)$ [219]. Interference effects reach their maximum around $\rho \sim 2\pi$, which defines the *intermediate size range* on a physical basis. Even in the scattering direction parallel to the incoming field, radiated fields *do not* sum up coherently due to the different optical paths across the particle. The phase lag between the forward-scattered field and the external field makes the normalized amplitude in the forward direction, $S(0)$, a nontrivial complex number. Then, the extinction cross-section, C_{ext}, is also affected as a consequence of the optical theorem [19,154,219]:

$$C_{\text{ext}} = \frac{4\pi}{k^2}\Re\mathrm{e}\ S(0) \tag{2}$$

where $\Re\mathrm{e}$ indicates the real part of the complex number. The dependence on particle features reaches its maximum in the intermediate size range. Two general cases can be distinguished, depending on whether the local internal fields are affected by the surrounding dipole elements in the particle. We will discuss these two opposite cases in the next sections.

2.1. Independent dipoles

If each dipole is forced by the incoming wave without being affected by its neighbors, then radiated fields have independent amplitudes while phase lags are dictated only by the incoming wave. The Rayleigh–Debye–Gans (RDG) approximation holds if the phase shift across the particle is small, $\rho \ll 1$ (either a, m, or both are small enough). Otherwise, the particle behaves in a peculiar fashion described by van de Hulst [219]: an analytical solution for $S(0)$ can be derived for uniform spheres

$$S(0) = x^2K(\mathrm{i}\rho) \tag{3}$$

where $x = ka$ is the size parameter and $K(z) = \frac{1}{2} + \frac{e^{-z}}{z} + \frac{e^{-z}-1}{z^2}$. Fig. 1 shows a plot of the complex amplitude in the forward direction (a) and the extinction cross-section (b; black solid line), the former normalized by x^2 and the latter to the geometrical cross-section, $G = \pi a^2$, plotted over a fairly extended range of ρ. Fig. 1(b) includes the Lorenz–Mie curves obtained for spheres with $m = 1.10$ and $m = 1.33$ (orange and blue, respectively). The figure illustrates the universal role of ρ as the running parameter that sets the forward complex amplitude (Fig. 1(a)) and, therefore, the extinction maxima and minima (Fig. 1(b)). For small ρ, internal fields suffer negligible phase changes, thus, constructive interference occurs in the forward direction (RDG approximation). In the

[1] While this formula is derived using the electrostatic approximation, it also applies to particles subject to electromagnetic waves (oscillating fields) for frequencies up to some orders of magnitude larger than that of visible light [2].

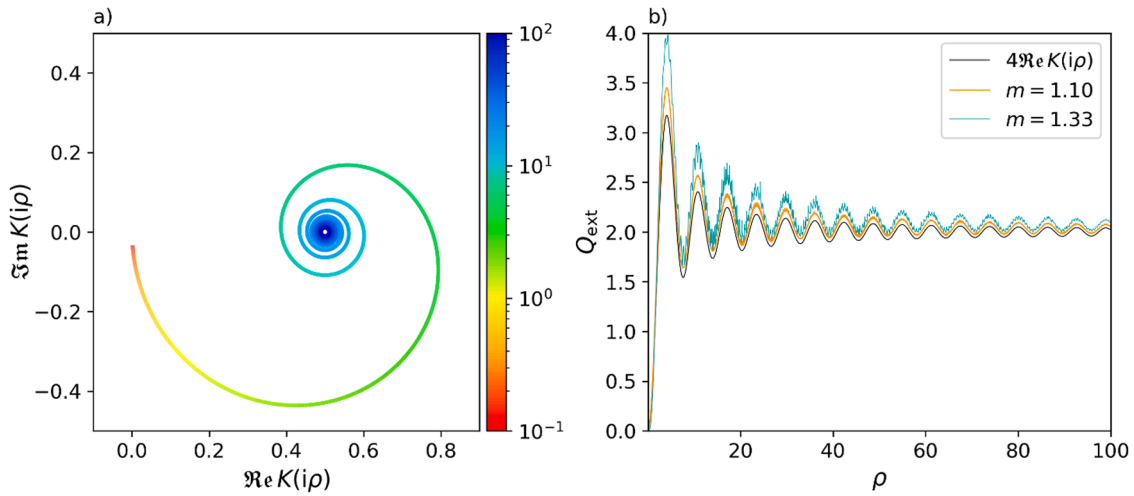

Fig. 1. Normalized complex amplitude $S(0)/x^2$ (a) as a function of the running parameter ρ from 0.1 to 100 (color bar, log scale) and (b) the corresponding normalized extinction cross-section $Q_{\mathrm{ext}} = C_{\mathrm{ext}}/\pi a^2$ (black solid line) compared with the results obtained for Lorenz–Mie spheres with refractive indices $m = 1.10$ (orange) and $m = 1.33$ (blue).

intermediate size range, the internal distribution of fields dominates [219]; much larger particles (ρ>>2π) contain several wave periods and most of the interference effects vanish (this is named anomalous diffraction regime by van de Hulst [219]). The oscillations of the normalized extinction cross-section (Fig. 1(b)), equivalently, in $\Re\mathrm{e}\ S(0)$, are due to alternating conditions of partially constructive and destructive interference between the emerging fields: a discussion of their origin and positions was given by Sorensen [202].

Fig. 1(a) also clarifies the relative role of $\Re\mathrm{e}\ S(0)$ and $\Im\mathrm{m}\ S(0)$: the latter dominates for small ρ encompassing the Rayleigh regime until the first minimum of $\Im\mathrm{m}\ S(0)$, the former dominates for large ρ and the extinction cross-section approaches the asymptotic value 2G (the region close to the center of the spiral). This result is known as the *extinction paradox* [219], namely, the capability of a diffractive object to remove twice the power intercepted by its geometrical cross-section. The intermediate size range corresponds to the crossover between these two limits, from red to green in Fig. 1(a), and represents a considerable theoretical and experimental challenge. Moreover, it is also the range where the normalized cross-section of a particle (Fig. 1(b)) reaches its maximum value, elucidating the reason why this size range is so important when dealing with the optical properties of small particles. An extension of this approach to non-spherical, non-uniform particles is given by Villa et al. [222].

Similarly to the forward-scattered field, the differential cross-section $F(\vartheta)$ becomes non-trivial as scattering at any angle ϑ depends on the internal field distribution [11]. Introducing the functionality for the refractive index as in the polarizability formula, $f(m) = |(m^2-1)/(m^2+2)|$, the differential cross-section expressed in terms of fluence, i.e., the differential cross-section multiplied by k^2 is:

$$F = k^4 a^6 f^2(m) \tag{4}$$

where $k = 2\pi/\lambda$ is the modulus of the wavevector. For small particles, F is isotropic except for the obvious asymmetry introduced by the dipole term. More generally, $F(\vartheta)$ can be conveniently related to the structure factor of the scatterer, i.e., the squared Fourier transform of the internal field distribution [203]. It is straightforward to relate a length scale L of the internal field distribution and the length probed by sensing the light scattered at angle ϑ, or even better the corresponding modulus of the scattering wavevector $q = 2\pi/L$. Under the elastic light scattering conditions, $q = 2k\sin\frac{\vartheta}{2}$, the scattering wavevector being the difference between the incoming and scattered wavevectors, $\vec{q} = \vec{k}_i - \vec{k}_s$. In other words, the internal field distribution affects $F(\vartheta)$ at a length scale corresponding to the limit of resolution for a collection optics having a numerical aperture $NA = n\sin\vartheta$. A powerful example of this approach and the corresponding results can be found in the realm of colloidal aggregates, where probing methods based on light scattering are vastly applied [61]. Due to the low optical thickness of aggregates, cross-sections are usually computed through the RDG approach [77, 203]. The position of each monomer determines the relative phase of the waves emerging in each direction so that the differential and total scattering cross-sections can be easily obtained by summing the scattered waves. Despite obtaining the cross-sections being technically simple, data interpretation in terms of the optical theorem requires a few more steps, as discussed in Section 3.

2.2. Interacting dipoles

We now discuss the case where dipoles affect each other. Large homogeneous spheres covered by the Lorenz–Mie theory provide a good example [19,219]. Under these conditions, even the forward scattering amplitude $S(0)$ is affected by the nontrivial internal field distribution: the forward-scattered fluence is reduced by interference compared to the Rayleigh and RDG cases, where all the dipoles radiate coherently at zero scattering angle [35]. Moreover, diffraction is enhanced as the phase shift parameter ρ increases: the diffracted wavefront is in phase quadrature with the incoming wave enhancing the interference between transmitted and diffracted waves [202]. The phase shift parameter also contributes to the scattering at an angle ϑ. It is worth introducing the so-called *homologous scattering diagram* obtained as a function of ρ and qa [219]. This means that $(m-1)$and ϑ vary proportionally to $1/qa$. The homologous scattering diagram unifies both the scattering matrix elements $S_1(a,m,\vartheta)$ and $S_2(a,m,\vartheta)$ into one function of ρ and qa, $(ka)^2A(\rho, qa)$. For $\vartheta = 0$ it provides $A(\rho,0) = K(\mathrm{i}\rho)$ (see Eq. (3)). Fig. 2(a) represents the modulus of the complex amplitude $A(\rho,qa)$ following van de Hulst [219]. Two expansions for the real part are adopted, for $\rho < 8$ and $\rho > 8$, using ten terms, while the imaginary part is analytical. The two approximations match smoothly. The homologous scattering diagram shows regular maxima, occurring for $qa \sim 5,\ 8,\ 11$ and so on. On the other hand, maxima and minima are almost equally spaced in ρ, following the sequence obtained for $\vartheta = 0$, that is for C_{ext}, although occurring in positions that depend on qa. In the limit of large ρ, the results for pure diffraction are obtained, showing that the internal field distribution plays a negligible role. We finally note that the phase shift parameter is proportional to the particle polarizability divided by $(ka)^2$ [172]: this is the same normalization adopted for obtaining $A(\rho,qa)$ from

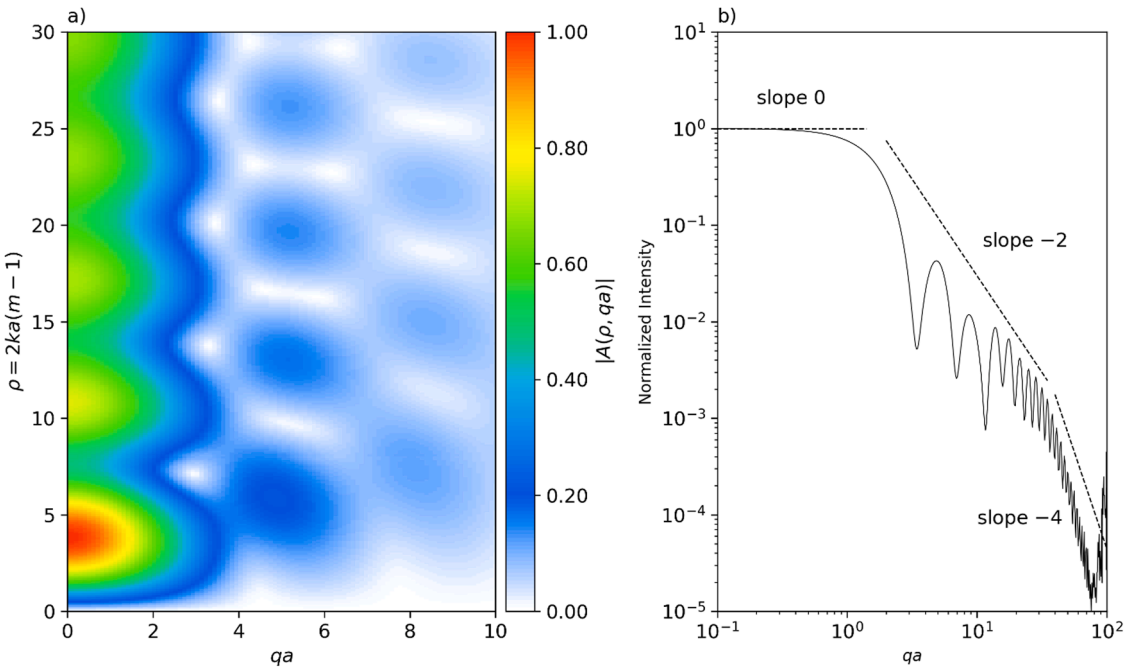

Fig. 2. (a) modulus of the amplitude $|A(\rho,qa)|$ for the homologous scattering diagram obtained by matching two approximations for $\rho < 8$ and $\rho > 8$. $A(\rho,qa)$ is the normalized complex scattering amplitude for optically soft spheres, while the dimensionless product qa gives the angular dependence. (b) universal behavior of the envelopes of the angular scattering diagrams obtained from Lorenz–Mie theory, with the forward scattering lobe ($qa < 1$), the Guinier transition around $qa \sim 1$, and the power law region, with spectral indices − 2 and − 4, as indicated. See Sorensen [202] for details.

$S(a,m,\vartheta)$.

The regularity evidenced by the homologous scattering diagram can be extended to the more general case of Lorenz–Mie analytical solutions. As recently introduced by Sorensen, a general framework to interpret Lorenz–Mie scattering in terms of quasi-universal laws can be derived. We briefly summarize the main physical quantities, methods, and results, referring the reader to the works published in the last two decades [14,83,92,204,206–208]. By analogy to the polarizability formula in Eq. (1), the term $(m - 1)$ is substituted by $f(m)$ to obtain the *internal coupling parameter* $\rho' = kaf(m)$ [11]. The fluence $F(\vartheta)$ is then normalized to the Rayleigh cross-section, $a^6k^4f^2(m)$, which is the same as normalizing to the square of the average particle polarizability [172], and its angular dependence is reported in terms of the dimensionless wavevector qa (hence the name "Q-space analysis"). In such a way, Sorensen shows that 1) angular scattering diagrams exhibit quasi-universality for any given ρ or ρ'; 2) the forward scattering lobe follows a quasi-universal curve if plotted against the phase shift parameter ρ or ρ'. Some relevant features arise from the Q-space analysis. The plot is divided into three regions for the envelopes of the Lorenz–Mie oscillations (see Fig. 2(b) for a sphere with $x = 50$ and $m = 4/3$ for water in air): i) the forward scattering lobe, for $qa < 1$, where the normalized cross-section is constant and the fluence is reduced compared with the Rayleigh ideal case; ii) the "Guinier" regime where the curves show a typical roll-off, for $qa \sim 1$; iii) two power laws $(qa)^\gamma$, with exponents $\gamma = -2$ and $\gamma = -4$. The latter recalls Porod's law, connecting the exponent to the space dimensionality d, $\gamma = -(d + 1)$ [203]. The transition between the two power laws in the scattering diagrams depends on the phase shift parameter and occurs at $qa \simeq 1.2\rho$. We stress that plotting normalized data as a function of the dimensionless size qa is similar to the approach adopted for small-angle light (or X-ray) scattering in colloidal physics. As in that case, the transition from the plateau at very small angles to the Guinier regime provides an estimate of the gyration radius R_G of the scatterer. By estimating the size of a sphere from the roll-off position and comparing this to its actual radius a, we obtain a curve whose oscillations taper for large ρ [172]. The positions of these oscillations are distinctly related to the oscillations in the forward-scattered field, therefore to C_{ext}. For large ρ, maxima and minima occur at angles as in Fraunhofer diffraction, the distance between two minima being related to the object size. Since the angular position of the maxima is almost independent of the refractive index of the sphere, it could be considered a sizing method for solid (large) particles [110,129,168]. The quasi-universal scattering diagrams bring an apparent paradox: for relatively large values of the phase shift parameter, $\rho > 5$, they nicely agree with a shell model for the field within the particle, but a detailed analysis of the internal fields does not agree with this simplified description [11,203]. Nevertheless, the scale lengths of field inhomogeneities within the particle (hotspots) correlate with the slope changes in the scattering diagram thus showing the physical origin of these features. Finally, still from the Lorenz–Mie solutions, Sorensen also found a remarkable quasi-universal curve if $F(0)$ is normalized and plotted against ρ or ρ' [202]. We will come back to this additional quasi-universal behavior in Section 6.

2.3. Non-spherical scatterers

The basic principles outlined above are roughly the same in the case of non-spherical objects with regard to the fields within a polarized object and the emerging fields. Nevertheless, similar optical properties can be due to different features of the scatterer, or conversely, small differences among scatterers may result in large differences in their corresponding optical properties. The inverse scattering problem becomes really challenging and requires knowing additional parameters to be solved. For example, it has been recently demonstrated that the sensitivity in measuring the light scattering profile, $F(\vartheta)$, of non-spherical objects such as blood cells is too low to characterize their shape effectively; additional information can be gathered from the complex Fourier transform of their scattering pattern [189]. While analytical solutions are not available [169], numerical methods are contributing to filling the gap of knowledge that still affects the description of non-spherical particles, especially in the intermediate size range. Two main approaches are adopted to evaluate the radiating fields, stemming from the evaluation of the internal field distributions

[182,233]: T-matrix (TM) [46,140–142,164,196,200,201] and Discrete Dipole Approximation (DDA) [182,236] can cover any particle typology [49,87,88,162]. Other approaches are effective with metallic particles [45,76,186]. Although computation is appreciably slow, an effective approach is the Invariant-Imbedding TM method (IITM) [101]. The same limitation applies to the Finite Element (FE) models [76,100] and the Finite Difference Time Domain (FDTD) [213]. Larger particles (tens or hundreds of the wavelength) can be modeled through geometrical or physical optics [124,212]. A general principle to choose the best approach is not available yet: these methods cannot be used routinely as their demand for computation resources may be impractical. Dedicated studies are required to optimize algorithms and provide the needed information in specific applications where inversion introduces additional difficulties.

2.4. Absorption

A few words must be spent about absorption, which makes the total scattering cross-section, C_{sca}, smaller than C_{ext} and the single scattering albedo $ssa = C_{sca}/C_{ext}$ smaller than unity [19,144,193]. Absorption is related to the damping in dipole oscillations, meaning smaller radiating fields and increasing phase lag. Since C_{ext} is affected by interference and absorption is essentially not, *ssa* inherits the same interference effects of C_{ext}. Of course, for non-ideal particles, *ssa* can be affected by other features such as shape, internal inhomogeneities, and surface roughness. The difficulties in measuring absorption are essentially due to the need to collect the scattered radiation over a large solid angle [58,108,155]. Typical uncertainties are around 5%, with different effects depending on the application one aims toward. Except for extremely absorbing materials like black carbon, *ssa* values are typically larger than 0.5: typical values for dust and aerosols are around $ssa = 0.8 - 0.9$ [120,155]. Therefore, a 5% error on a *ssa* of 0.90 amounts to a 6% error in C_{sca}, which is acceptable for many applications. The same error on *ssa* would represent a 100% error in $C_{abs} = C_{ext}(1 - ssa)$, which provides information about the power absorption by the particle. We will come back to black carbon in Section 7, while *ssa* will be considered again in Section 8.

3. The need for multiparametric analysis on single particles

Single-particle light scattering methods ease data interpretation since the ill-posed problem of disentangling mixed contributions from different scatterers is avoided by design [132]. Generally speaking, single-particle measurements are more complicated from the experimental point of view since noise limits the detection of faint signals due to small cross-sections. This typically requires focusing the light beam onto a particle, using high-sensitivity sensors, and taking into account the transit position through the beam, which in most cases is not uniform in intensity. The workarounds for the latter issue are outside the scope of this work. They sometimes require statistical or deconvolution approaches that limit the advantages of working with single particles to some degree, as with the Optical Particle Counters (OPCs) [226]. In the following, we will assumethat we are working with scattering data collected with fine control of the intensity (or even the field), impinging upon each particle, regardless of the method.

Extinction and scattering at one or more angles or wavelengths are still the most commonly and easily measured quantities. However, when SALS is operated on single particles, the low scattered power causes significant limitations [5,6,57,58,75,106,190,191,227]. Fast multipixel detectors like photodiode arrays and CCD/CMOS cameras currently allows the implementation of methods exploiting the simultaneous detection of scattered intensity values. Examples can be found both in SALS applications [59] and with the two-dimensional angular optical scattering (TAOS) [90], or even for the time-resolved correlation (TRC) [31]. Optical trapping spectroscopy also proved effective [33,75,225], as did holographic methods using in-line [12,15,37,68,112,183] and with off-axis optical schemes [38,119,238].

Let us now overview and compare the most common and simple single-particle methods. The OPC measures the power scattered within a large solid angle around 90° (Fig. 3(a)), whereas measuring the power removed from the beam is the basis for the Single Particle Obscuration Sensor or Single Particle Optical Sizing (SPOS, Fig. 3(b)) [13,161]. The OPC works with a focused laser beam, whereas the SPOS uses a highly astigmatic sheet of light to illuminate the whole volume through which the sample is flown. The former can reach a remarkably higher sensitivity than the latter, down to 200 nm compared to 1 μm in diameter for latex spheres, on the other hand, in SPOS, particles are uniformly illuminated to avoid having to compensate for intensity variability. OPC and SPOS methods are designed to measure different optical properties, C_{sca} and C_{ext} respectively. Both methods are simple, cost-effective, and easy to use, thus they are widespread in Science and Industry. As mentioned previously, they are covered by three specific ISO standards [95–97]: the first two aim at characterizing airborne particles, whereas the third is for liquid suspensions.

It is worth pointing out the advantages of SPOS measurements over OPC in terms of scattering fundamentals [13,161]: SPOS directly provides C_{ext} with a unique configuration that can rigorously obtain a *total* cross-section experimentally. Let us then interpret extinction in terms of the optical theorem [154,219]. As we have seen in the previous section, $S(0)$ is the result of the superposition of fields with phases that are only dependent on the phase distribution within the particle. Three basic considerations should be made: i) $S(0)$ is related to the *effective* polarizability of the particle, which is also related to its volume; ii) the influence of particle shape and internal inhomogeneities are reduced to a minimum as the angular resolution of the light collection geometry vanishes at $\vartheta = 0$; iii) the optical theorem shows that information about $S(0)$, a *field amplitude,* is rigorously obtained by measuring C_{ext}, a *power* measurement. The field amplitude $S(0)$ depends on size less than fluence $F(0)$ does, so it covers a more extended size range (with a smaller resolution). Therefore, SPOS gives one of the least possible model-dependent particle characterizations.

Both OPC and SPOS rely on measuring one optical parameter to infer size, therefore, are especially prone to the limitations discussed above; setups with a combination of both methods have been proposed to overcome them [229]. The main reasons for the lack of practical implementations of such hybrid solutions are attributable to difficulties in cross-calibrating the two channels. While uniform spheres have their scattering defined by a pair of parameters (size and refractive index), this is not the case for almost all the particles encountered in practice. The very concept of size is not well defined for non-spherical shapes, making sizing unreliable [29,71,82,123,171,198,226,231]. The same signal can be related to different combinations of the particle features, influencing sizing (see the discussion about the applications of light scattering by van de Hulst [219], chapter 18.4). Furthermore, measuring the refractive index of non-spherical particles is complicated by the contribution of shape, orientation, and inhomogeneities, which affect both scattering and extinction appreciably [26,109]. Real-case samples measured with the two methods will give two different size distributions, each according to its own definition. At least one of them will be misleading if used interchangeably or out of context. As a matter of fact, cross-calibrating OPC and SPOS is ultimately impossible except for ideal spheres of known composition. Moreover, which method gives the correct measurement cannot be known *a priori* without any other independent knowledge of the sample (ideally speaking, of each measured particle). Chesler et al. [26] and Simonsen et al. [198] discuss some examples of such limitations based on specific measurements in comparison with an independent, non-optical method providing the volume of single particles immersed in an electrolyte (resistive pulse sensing, or Coulter method).

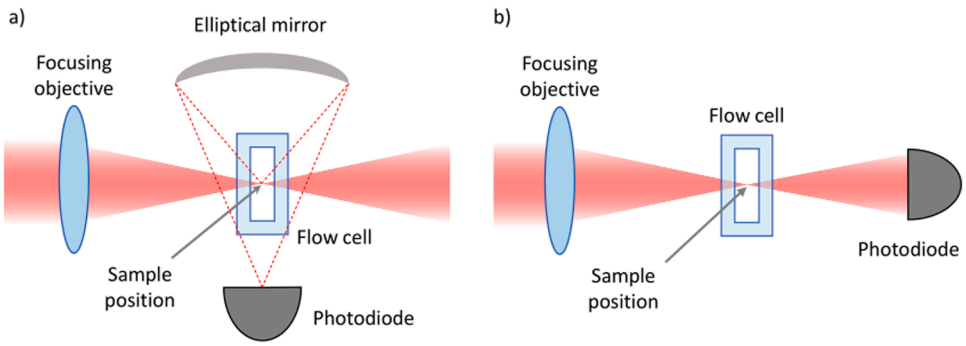

Fig. 3. Schematics of the OPC (a) and SPOS (b) methods. In (a) the light scattered by a particle within an extended solid angle impinges onto an elliptical mirror and is focused onto a detector. In (b) the power of the light beam impinging onto the detector is attenuated by the presence of a particle.

4. The complex forward scattering amplitude $S(0)$

We now focus on the complex forward scattering amplitude, $S(0)$, and show how it can be used to characterize non-ideal particles, especially in the intermediate size range. The condition $\vartheta = 0$ entails a simplified perspective on the particle properties (Section 2). All the dipoles forced by the incoming field radiate fields with phases that compensate the phase lag of the forcing field accumulated along the propagation axis. Irrespective of the distribution of dipoles within the particle, the emerging field is the sum of the complex amplitudes. The fact that makes forward scattering peculiar is that this occurs *only* in this direction. The same principle also explains how the total extinction cross-section of a particle, C_{ext}, is accounted for by the field amplitude scattered in the forward direction and underlies the optical theorem. The combination of increasing amplitude, changing phase, and shrinking forward scattering lobe perfectly match the behavior of the complex field, power, and differential and total cross-sections [19,154,219].

We can explain in more general terms how $S(0)$ inherits the features of the particle. $S(0)$ can be better understood by considering the correlations of the elementary emitters in the particle, i.e., an ensemble of N arbitrarily small dipoles [34,160]. This description is also related to what is discussed by Sorensen et al. [208]. Let's describe a particle of radius a as composed of a set of elementary domains, each emitting an elementary wave excited by a local field. In this framework, which means including the "radiation reaction" [160,230], each domain is likened to a scatterer whose polarizability is given by the Lorentz–Lorenz formula in Eq. (1). Without losing generality, let us limit ourselves to purely dielectric materials so that α is real. Under the RDG approximation, the forward scattering amplitude $S(0)$ is then purely imaginary:

$$S_{\text{RDG}}(0) = -\mathrm{i}N\alpha k^3 \tag{2}$$

$N\alpha$ can be interpreted as the effective polarizability of the particle. As expected from the constraint on phases, no information is encoded into $S(0)$ about the positions of the elementary emitters. The total radiated field is then proportional to the particle volume multiplied by $f(m)$, which is the optical density of the material. Structural features like shape and internal structure are not considered in this approximation, as a level of detail that the model gives up in exchange for an equally significant simplification. However, this also brings in an inconsistency. Under the hypotheses of non-absorbing arbitrarily small emitters in the particle, the scattered amplitude in Eq. (2) is purely imaginary, thus implying a vanishing cross-section in force of the optical theorem Eq. (2). A workaround consists in calculating both the scattering and absorption cross-sections explicitly, as in RGD theory, or by using the arguments and formalism for the complex field suggested by Parola et al. [160]. In the following, we sum up the implications of this argument in the case of scatterers limited in space [34]. With the hypothesis of elementary emitters that are arbitrarily small, we can expand $S(0)$ to the next order in the dimensionless quantity $N\alpha k^3$:

$$S(0) = -\mathrm{i}N\alpha k^3 + C_1\left(N\alpha k^3\right)^2 + \mathrm{i}C_2\left(N\alpha k^3\right)^2 \tag{3}$$

For simplicity, here we consider a real α, but the expansion can be generalized to complex α if the expansion term remains small. The two constants of the expansion, $t = q/2k$, have the expressions:

$$C_1 = 2\int_0^1 \mathrm{d}t\; P(qa)\left[t - 2t^3 + 2t^5\right] \tag{4}$$

$$C_2 = \frac{2}{\pi}\int_0^\infty \mathrm{d}t\; P(qa)\left[4t^4 - \frac{8}{3}t^2 + \left(t - 2t^3 + 2t^5\right)\ln\frac{|t-1|}{t+1}\right] \tag{5}$$

where $P(qa)$ is, by the Wiener–Kintchine theorem, the Fourier transform of the two-points correlation function describing the statistical properties of the emitters within the particle. Eq. (3) includes two more terms than Eq. (2): the real part and a second-order correction to the imaginary part. Both contain the correlations between the elementary emitters through the corresponding Fourier transform. Eq. (3) highlights how the features of the particle are encoded into the real and imaginary parts of $S(0)$ and indicates a boundary of validity of the RDG approximation [34,203]. At the first order of the expansion, $S(0)$ is given by the imaginary leading term, while the second-order real term is responsible for the phase lag of the emerging wavefront. This causes extinction, related to the polarizability distribution within the particle and the way radiation is scattered.

It is worth making a short comment about the sum of the elementary field amplitudes at an arbitrary angle. Although apparently easier to handle than the second-order term, it ultimately contains the same physical elements. By summing all the elementary fields over a solid angle to evaluate the scattering cross-section, one obtains an expression that is formally the real part of Eq. (2) [61,208]. In fact, the forward-scattered amplitude $S(0)$ is closely related to $P(qa)$, the Fourier transform of the correlation function (the angular power spectrum), or the angular scattering intensity distribution $F(\vartheta)$, commonly measured in light scattering (SALS or MALS). This also implies that the sum of the complex fields at any angle reveals $\Re\mathrm{e}\; S(0)$ through the differential extinction cross-section, while the sum of the intensities at $\vartheta = 0$ gives the forward-scattered intensity, thus the modulus of the forward-scattered field led by the first-order term. Under the RDG approximation, this is $\Im\mathrm{m}\; S(0)$.

Summing the elementary fields to evaluate the scattering cross-sections is a common practice in the field of colloidal aggregates, where the field radiated by each monomer in the aggregate is assumed not to be affected by the surrounding monomers, and the forcing field is undisturbed as in the RDG approximation [203]. The forward scattering amplitude $S(0)$ of an ensemble of particles can be recovered from the experimental results reported by Ferri et al. [61] following a modified

Carr–Hermans approach [22]. A different approach has been given by Potenza et al. [175].

We finally remark that, when dealing with optical theorem arguments, one needs to expand to the next order to explain the scattering properties described by the first-order term [34,175,219]. Other than the real part accounting for extinction, another example has been given for depolarized light scattering [42]: the first-order term is depolarized and cannot interfere with the transmitted wave whereas the *polarized* term in the second-order term can. Understanding the separation of these two synchronous terms led to a simpler procedure to perform dynamic depolarized light scattering measurements in the forward direction [40,41,176]. An extensive discussion of the depolarized light scattering from fractal aggregates can be found in the work by Sorensen [203] and references therein. The complex forward-scattered amplitude can then be considered as a reference for understanding the particle features thanks to the peculiar behavior of the fields in the direction of the incoming wave. If we consider the homologous scattering diagram in Fig. 2, we can argue that there is an evident relation between $S(0)$, or the equivalent normalized $A(0)$, and the corresponding angular scattering distribution. At any given ρ, maxima in $A(\rho, 0)$ along the vertical axis correspond to smaller values of $A(\rho, qa)$ over the entire q range. Similarly, minima in $A(\rho, 0)$ are followed by higher secondary lobes of $A(\rho,$

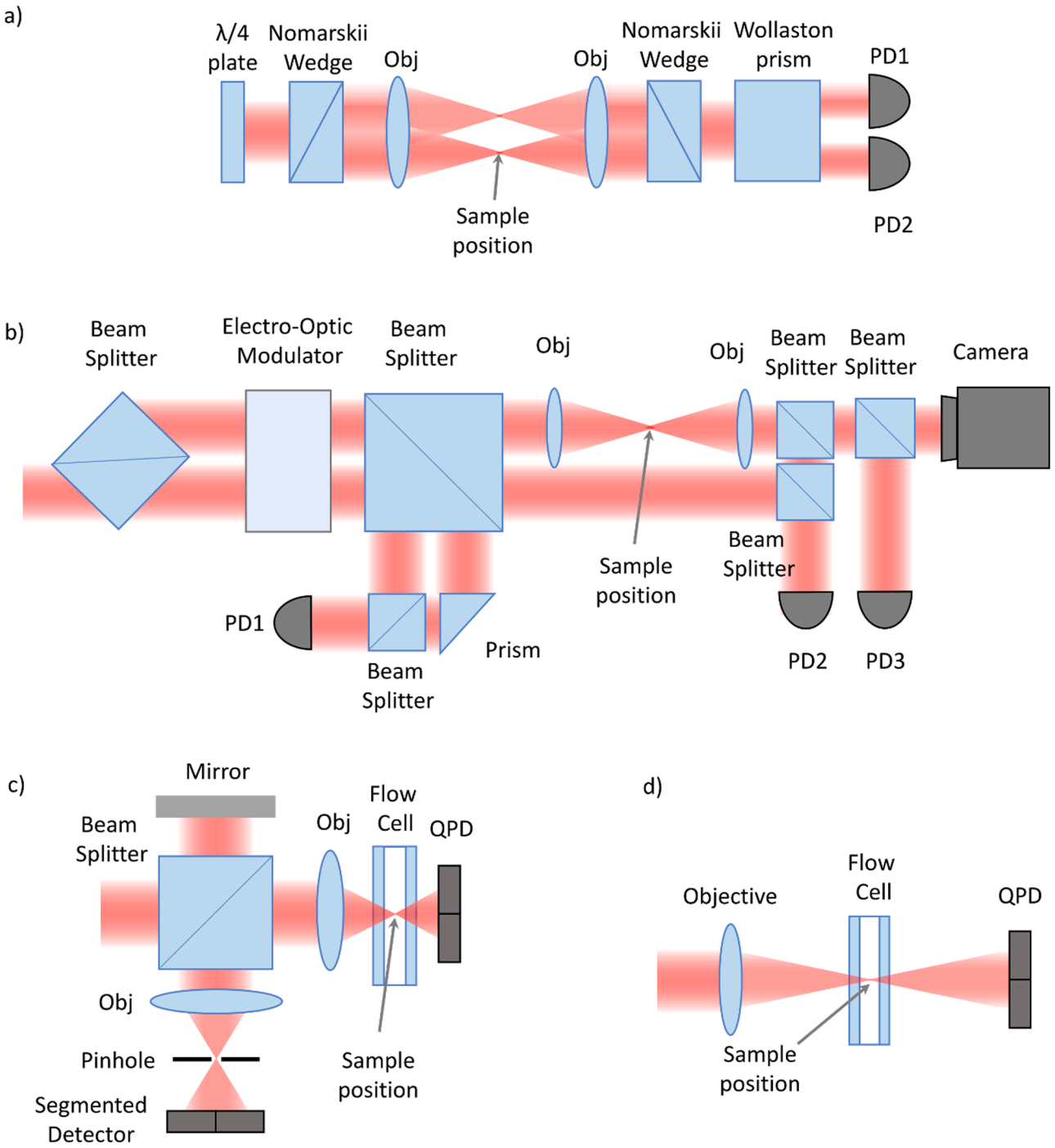

Fig. 4. Schematics of the methods to characterize nanoparticles by interferometric measurements of the scattered field amplitude used by (a) Batchelder and Taubenblatt [8,9,214]; (b) Bassini et al. [7]; (c) Ignatovich et al. [94]; (d) Giglio and Potenza [73]. Obj: objective (typically high NA); PD: photodiode; QPD: quadrant PD.

qa). The diagram in Fig. 2 also highlights the uniformity and regularity over an extended range of its parameters. A similar uniformity is obtained by the aforementioned Q-space analysis introduced by Sorensen. Although the detailed trend of $F(\vartheta)$ cannot be inferred from just $S(0)$, it sets a constraint on its integral that could help in interpreting data from ensembles of particles, for example, as it is for many cases of interest in practical applications.

5. Measuring $S(0)$

While the ability to infer particle properties from optical measurements needs a multiparametric approach, the real and imaginary parts of the forward scattering amplitude, $\Re\mathrm{e}\ S(0)$ and $\Im\mathrm{m}\ S(0)$, deliver information simpler to use than any other pair of parameters. $S(0)$ is a good choice to characterize a particle, especially if a single-particle method is adopted, because of the information embedded in its two terms that can be interpreted without depending on a model. They highlight discrepancies from ideal uniform spheres, as well as the effects of the refractive index n. For example, for particles covered by Lorenz–Mie theory n can be recovered from the distribution of the $S(0)$ data and improve sizing. Some examples of such applications [174] will be the subject of Section 6.

None of the early, now well-established, scattering methods provide the forward scattering amplitude for two main reasons. Measuring $S(0)$ requires isolating the transmitted beam and, more importantly, requires measuring the phase, Arg$S(0)$, which can only be done simultaneously by interferometric methods. Several techniques based on multipixel sensors, such as phase contrast microscopy, digital holography, and tomography, produce interferometric patterns that can be analyzed quantitatively to recover the scattered wavefront and, for example, the refractive index distribution of the imaged object [13,25,111,156,165,183,215]. These methods have been undergoing fast development and wide use, bolstered by the evolution of multipixel sensors and computation power. Here we focus our attention to methods based on smaller sensors like photodiodes (PDs) capable of much faster data acquisition, with corresponding statistical and experimental robustness.

The first method to measure the forward complex field amplitude dates back to the late '80s at IBM, stemming from the need to qualify the purity of liquids for industrial applications. Batchelder and Taubenblatt exploited a Nomarskii interferometer (see Fig. 4(a)) to measure water-suspended nanoparticles down to tens of nanometers in diameter [8,9,214]. The method was patented thanks to the capability to operate in-line on industrial liquids. In the late '90s, Bassini et al. [7] introduced a modified Mach–Zehnder interferometer (Fig. 4(b)) that provided precise measurements of the phase lag introduced by polystyrene nanoparticles on a glass slide, in the range 200–1000 nm where the phase changes appreciably. Half a decade later, [94] combined a self-reference interferometric scheme of the forward-scattered wavefront to localize particles within a tightly focused laser beam, and a backscatter scheme (Fig. 4(c)) to generate background-free signals and increase the sensitivity down to 10 nm in diameter. In the meanwhile, Giglio and Potenza developed the so-called Single Particle Extinction and Scattering (SPES), operating a self-reference interferometric scheme in the forward direction (see Fig. 4(d)). The system was designed following technical simplicity and the capability to work in-line with liquids and gasses, and has been patented [73,178]. SPES includes a segmented photodiode downstream of the sample (QPD); it is robust and fast enough to manage time-resolved signals even with high flow rates over a large range of signal amplitudes, relying on its extended dynamics. We refer to the published literature for technical details and the slight variations of the setup based on the same method [146,178]. Among the others, this is the only scheme exploited so far for

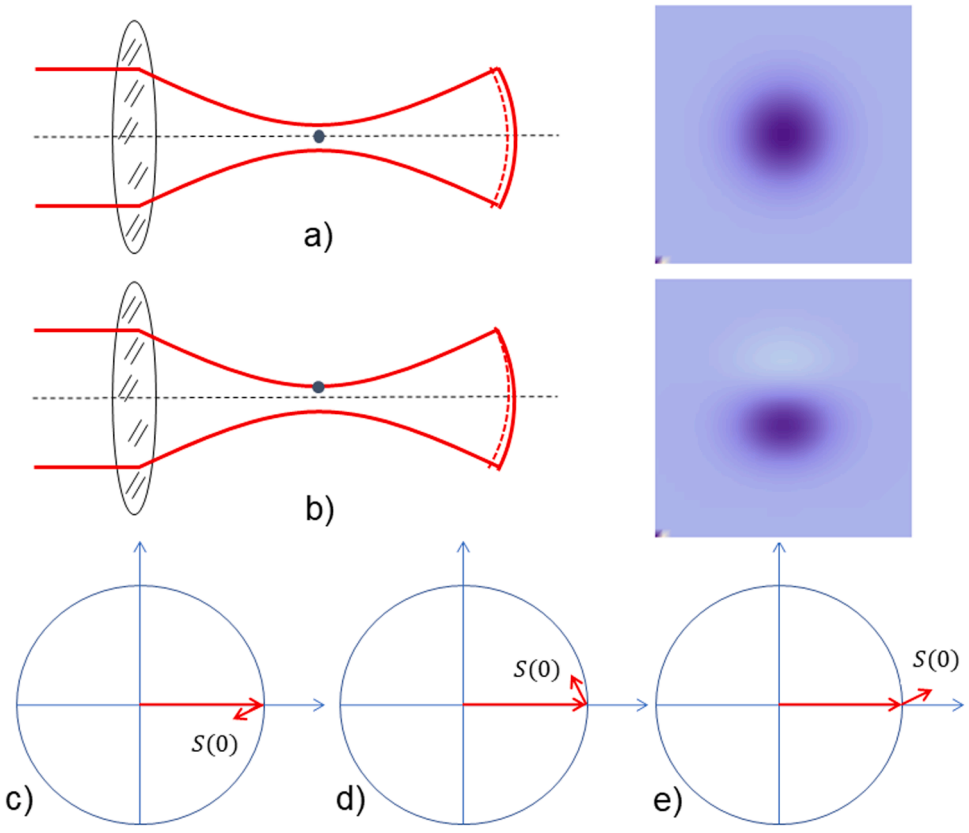

Fig. 5. Schematic of the SPES physical processes underlying the technique. A particle in the plane of the beam waist sitting on the optical axis (a) and shifted off-axis (b). The emerging waves (dashed red lines) interfere with the transmitted wave (solid red) giving the intensity distributions reported on the right. In (c), (d), and (e) the phase relations between the phasors are reported.

characterizing particles in a variety of fields both for scientific and industrial purposes.

We give a brief description of the fundamentals of the SPES method referring to Fig. 5. A laser is focused into the region where the particles are driven by a laminar flow (scattering volume), to pass through the beam generating a scattered wavefront. When the particle is at the center of the beam waist (Fig. 5(a)), the scattered wavefront is concentric with the transmitted beam diffracting from the beam waist. The emerging wavefronts are then homothetic, which makes the intensity measured downstream of the scattering volume independent from the longitudinal position where the sensor is placed. Moreover, at any transversal position on a plane downstream of the particle, the phase shift between the two waves is uniform and the transmitted beam is uniformly attenuated (see the panel on the right). When the particle is displaced from the optical axis (b), still in the plane of the beam waist, the two waves are partially skewed: interference causes the intensity distribution to be unbalanced on opposite sides of the transmitted beam (right panel). The corresponding combination of the phasors is schematically described in panels (c), (d), and (e) for the bottom, center, and upper parts of the interference pattern, shown in (b). It can be proven that the first measure (particle at center) rigorously gives the extinction cross-section, which is the real part of $S(0)$, while the latter provides the imaginary part for a proper displacement from the optical axis [73]. The combination of the two gives the complex amplitude without any free parameter. For instance, the combination of the phasors reported in panels (c), (d), and (e) of Fig. 5 for the particle as in (b) corresponds to the upper, central, and lower parts of the intensity distribution, respectively.

From a theoretical point of view, SPES is a practical implementation of the theory leading to the optical theorem applied to one particle. A key point is that the emerging wave scattered from one particle is in phase quadrature with the forward-scattered wave generated by several scatterers [19,143,154,219]. The phase lag for one particle is only apparently different from that of many particles. In the latter case, the forward-scattered wavefront is generated as a superposition of the fields scattered by each particle, which introduces a double Fourier integral: the overall wavefront is phase lagged by $\pi/2$ compared to the incoming plane wave. On the other hand, the wave emerging from a single particle does maintain the phase, but the phase of the transmitted beam is *advanced* by $\pi/2$ because of the (half) Gouy phase shift. This means that the same phase relation is obtained even with one particle following the optical theorem along an alternative path.

6. Examples

Different devices based on the SPES method have been used in recent years, as well as different approaches to analyze data [73]. We performed a wide campaign for testing potential applications in a variety of fields, evidencing the advantages and disadvantages of the method compared to sizing instruments. Moteki [145,146] has recently realized a SPES device, analyzing the method in detail and applying a specifically developed statistical analysis that widens its range of applications. Other groups are applying SPES to different characterizations, from nano plastics to dust in ice cores [232]. Here we review some applications of the method, reporting experimental data to exemplify the kind of information achievable beyond sizing, or *before* sizing [179]. Data are obtained from the same measurements reported in the literature we refer to; therefore, they are statistically identical to those already published or in some cases obtained from ancillary measurements. Results obtained with different SPES devices are reported for samples with particles both in liquid and air, emphasizing the additional information contained in raw data and the constraining parameters for data analysis and interpretation. We show evidence that such a characterization of single particles, or a population of particles, allows us to infer solid information in a model-independent way. With some examples, we show that once the data are examined with a proper interpretation frame, inverting size provides more reliable results. This is one of the reasons that originally motivated the development of the SPES method, as discussed in earlier works [174,179]. In analyzing data from real samples with non-trivial particles, we point out that considering two independent parameters discloses some issues. The variability of the refractive index affects the experimental results, as do deviations from the ideal uniform sphere and internal mixing such as coating, agglomeration, and so on. While a hierarchy of the contribution of each parameter to the signal is impossible, rigorous constraints to interpret data can be easily evidenced from raw data [198]. In general, independent information is needed about the individual particles, possibly about the entire sample under study, or a population among those composing the sample.

We present data as two-dimensional histograms where colors indicate the number of particles detected within a given bin; the corresponding color scale is reported on the right. Abscissas and ordinates are $\Re\mathrm{e}\ S(0)$ and $\Im\mathrm{m}\ S(0)$: they essentially consist of the raw data from the instrument, obtained from the beam attenuation (with the faint forward-scattered power) when the particle is on the optical axis (Fig. 5(a)) and the intensity unbalance with the particle displaced (Fig. 5(b)) [178]. Both scales are logarithmic. Size polydispersity causes a distribution of values for $S(0)$ so that, roughly speaking, the smaller particles populate the lower-left corner of the plots.

6.1. Uniform spheres and isometric particles

Liquids with calibrated refractive index (Cargill Labs) have been used to form several samples of oil-in-water microemulsions. Fig. 6 reports the experimental results obtained with two samples, with refractive indices $n = 1.40$ (a) and $n = 1.50$ (b), respectively. Plots have been obtained by merging data from two instruments operating over two complementary size ranges. The two plots exhibit a clear difference between the populated regions. Micrometric droplets are as close as possible to homogeneous spherical particles and Lorenz–Mie theory curves can be used to fit the data. We obtain values in good agreement with the expected refractive index. Since there are no other free parameters, one can safely proceed with particle-by-particle size inversion. Notice that inverting from C_{ext}, $\Im\mathrm{m}\ S(0)$, or $F(0)$ is equivalent if the refractive index is measured, using a tailored inversion curve from Lorenz–Mie theory. Figs. 6a and 6b show the bias caused to sizing by an inversion curve based on a different refractive index. The latter is the case of a number of instruments, accurately calibrated with polystyrene spheres as is the case of the aforementioned ISO standards [95–97].

Characterizations of water emulsions and airborne droplets from $S(0)$ are discussed in Mariani et al. [127] and Potenza et al. [178]. Exploiting the high throughput of the method, populations of some tens of thousands of particles have been compared from different samples with similar polydisperse distributions peaked around 500 nm in diameter. In the work by Giglio and Potenza [73], discrepancies between the refractive indices have been measured down to a few percent, thus distinguishing polymeric particles with and without an added drug. The same analysis applies to similar particles provided that the effect of shape on the forward-scattered field is negligible. Note that this condition mainly depends on size but much less on composition: particles much smaller than the wavelength fall within the Rayleigh regime so their scattering properties essentially depend on their volume. In contrast, major effects can be detected in larger particles.

An example has been reported for industrial slurries from chemical-mechanical polishing of semiconductors, composed of a water suspension of CeO_2 nanoparticles [177,179]. Almost one million particles have been analyzed in a few minutes; the observed refractive index is around 2 and particles are very close to isometric shape as confirmed by transmission electron microscopy. Therefore, the spherical approximation can be adopted [109,174]. In the $S(0)$ plane, Ceria nanoparticles are distinguishable from pollutants with a lower refractive index (about 1.4). The size was inverted separately for each population according to the measured refractive index; the diameter distribution peaked at 180

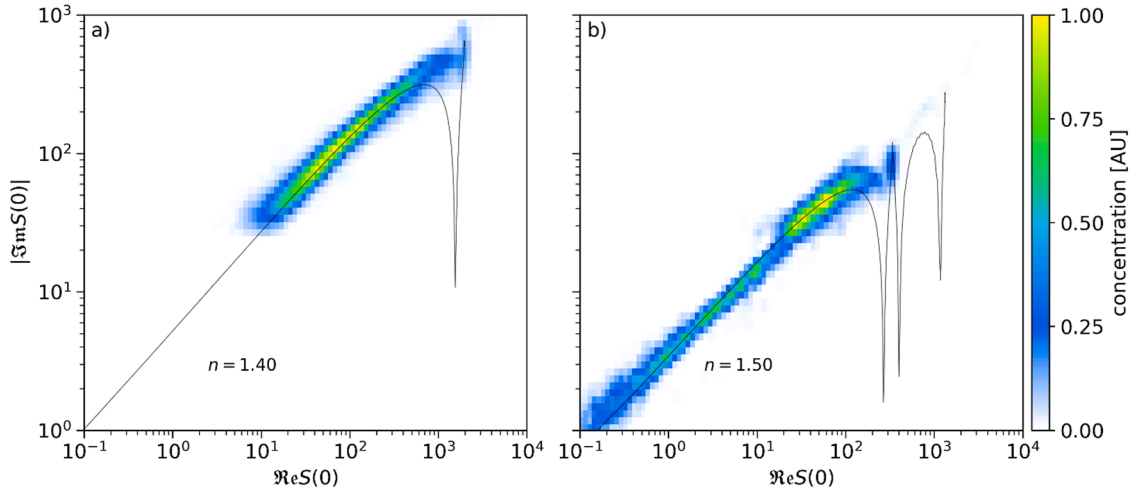

Fig. 6. Experimental results obtained with two water emulsions (histograms) of oils with calibrated refractive indices $n = 1.40$ (a) and $n = 1.50$ (b), compared with the expected Lorenz–Mie curve (black solid lines). Data from Potenza and Cremonesi [172].

nm, in accordance with the slurry specifications. We stress that the higher the refractive index, the smaller the minimum detectable particle. In another example, after injecting polystyrene nanospheres into mice, the serum and blood were analyzed with a SPES device. Nanoparticles were successfully separated in all cases including the unfiltered, non-diluted whole blood, enabling the study *ex vivo* of their evolution [194].

Spheres are ideal to check for the validity of the Sorensen quasi-universality discussed above. We recently produced Sorensen plots of our experimental results and obtained good agreement in comparing data with theory [198]. Oil-in-water emulsions are used to produce spherical droplets, and we don't have any free parameters to interpret data in terms of Lorenz–Mie theory; the normalization $a^6k^4f(m)$ and the phase shift parameter ρ, or ρ', are set as well. In Potenza and Cremonesi [172] we also report the results from airborne water droplets. Furthermore, we attempted to put on the same plot experimental results obtained with non-spherical particles and aggregates. As expected by Sorensen, the results are in sharp contrast with expectations for spheres. This makes such plots a relatively simple method to check for the validity of the spherical approximation and give a quantify deviations from it.

Some intricacies arise when absorption is not negligible, as the imaginary part of the refractive index is added to the scattering parameters. Together with its real part and the size of the particle, there are three unknowns and only two independent parameters in $S(0)$. In principle, this requires some independent information about the material; however, there are cases when the contribution of absorption can be disentangled from scattering. For example, if the imaginary part is much larger than the real part, the $S(0)$ values will be concentrated within a region that is incompatible with any dielectric material. This has been observed for Ag nanoparticles 100 nm in diameter [73]. In the presence of absorption, the appreciable increase in $\Re\mathrm{e}\ S(0)$ also increases sensitivity of optical instruments compared to the dielectric case. Instead of being negligible, it can be comparable to, or even larger than, $\Im\mathrm{m}\ S(0)$, as a result of the contribution of C_{abs} to C_{ext}. The inversion should then be preferably performed from $F(0)$, or $|S(0)|$, instead of $\Re\mathrm{e}\ S(0)$ or $\Im\mathrm{m}\ S(0)$.

6.2. Non-spherical particles

Beyond the realm of spherical particles, there is not a unique geometrical definition of size, but rather multiple case-specific size definitions that can hardly be compared. Moreover, when the optical response of an instrument is affected by the shape of particles, their orientation also plays a role. The increased number of parameters makes data interpretation correspondingly harder, although particles much smaller than the wavelength under the Rayleigh approximation are less affected by these effects. For larger particles, orientation causes a spread in optical parameters, over ranges that mainly depend on the aspect ratio. We report an example of the $S(0)$ distribution in Fig. 7(a) for oblate mineral dust particles (monophasic sample of Kaolinite) suspended in water. The evident spread is extended over half a decade in the vertical direction and hampers the inversion of the refractive index from the vertical distribution of the data. Moreover, by comparing data to Lorenz–Mie curves (see the solid lines in Figs. 7(a) and (b), refractive indices are in the caption) the effect of shape on the effective refractive index becomes clear [109]. In addition to spreading the distribution, non-spherical shapes produce a vertical shift, another indication of the non-ideality of the particles. Even in this case, inverting from $F(0)$, $|S(0)|$, $\Re\mathrm{e}\ S(0)$, or $\Im\mathrm{m}\ S(0)$ introduces relevant inconsistencies. On the other hand, discrepancies could be exploited to identify and then quantify deviations from the spherical approximation [198].

To distinguish oblate from prolate objects, we have exploited the shear of the flowing water through the cell, thin enough to orient particles along preferable directions imposed by the flow as shown by Villa et al. [222]. A mathematical description of such a hydrodynamic system requires checking the validity of many assumptions, so we opted for experimental proof of the particle orientation by using dumbbells with a size in the range of interest. A thorough formulation can be found in the work by Jeffery [99]. In Fig. 7(b), prolate particles of monophasic quartz clearly show the effect of orientation, as expected. We compare experimental results to numerically computed $S(0)$ values for several hundreds of thousands of particles with different shapes, aspect ratios, sizes, and refractive indices. To this aim, we ran the DDA code on multiple CPU and GPU computational platforms [236].

Metallic particles generally exhibit peculiar scattering effects due to surface plasmon resonances. Some typical examples are gold nanoparticles of different shapes, spherical, branched, and rod-like, inducing different resonance frequencies of the surface plasmon [173]. A corresponding change in the scattering properties, which can be distinguished clearly, separates the populations in the $S(0)$ plane.

7. Internal mixed particles and aggregates

Another feature to consider when interpreting scattering data is internal mixing, clustering, and aggregation. This is often approached through the mean field approximation (MFA) to evaluate the particle polarizability, to be inserted into the Lorenz–Mie model [19,30,219,

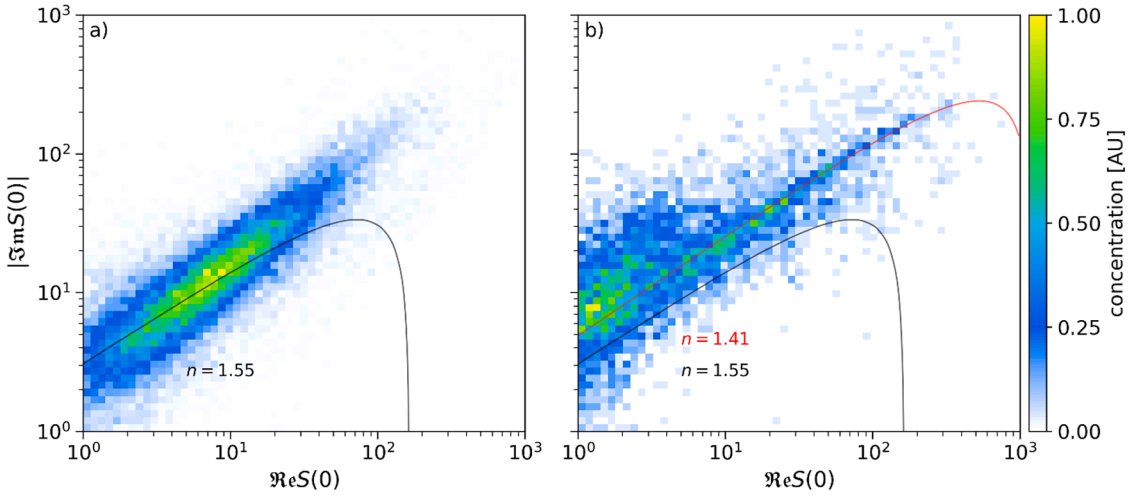

Fig. 7. Examples of experimental results obtained with non-spherical particles whose orientation is partially constrained by shear imposed by the water flow through the scattering cell. Two monophasic mineral samples have been used: (a) Quartz in (prolate), (b) Kaolinite (oblate). Black and red solid lines represent the Lorenz–Mie curves calculated for $n = 1.55$ and $n = 1.41$ respectively. Data from the study by Villa et al. [222].

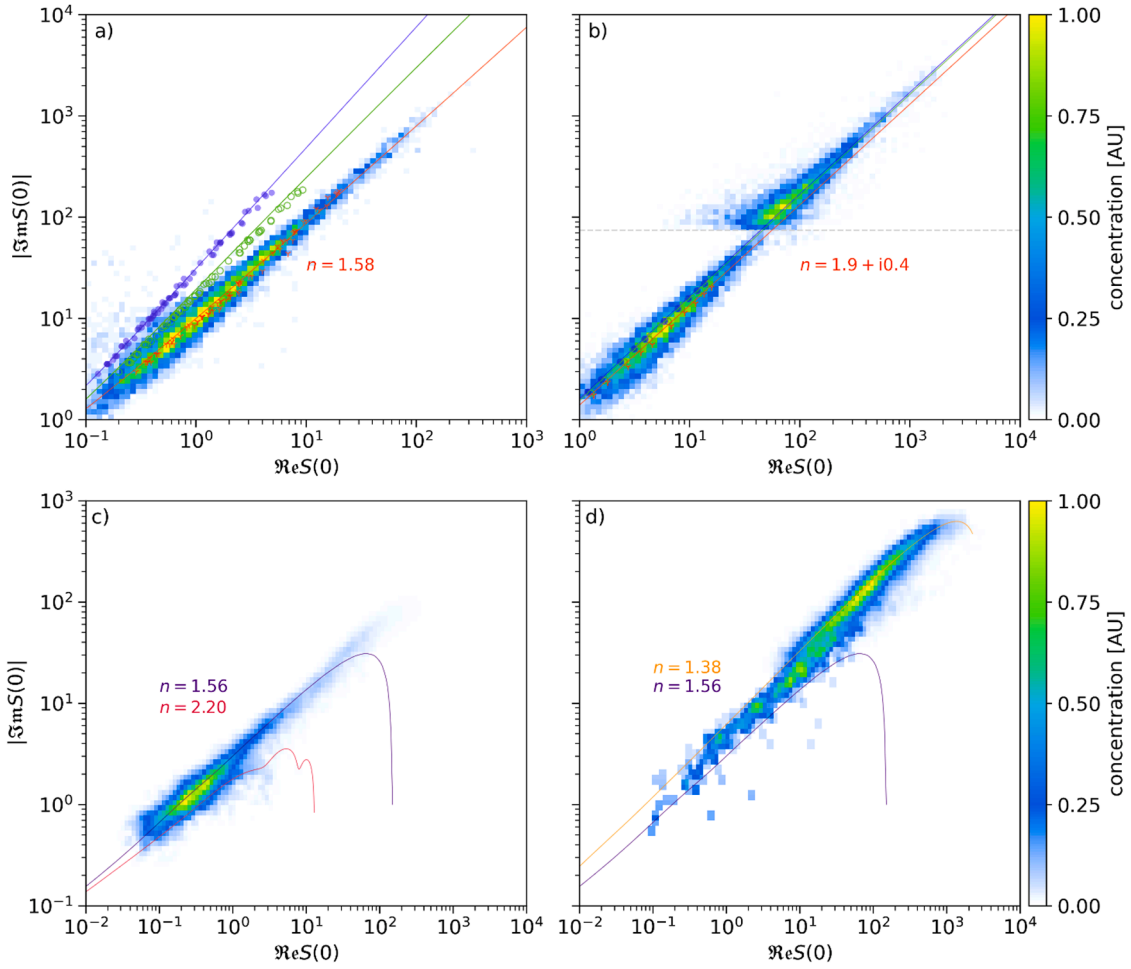

Fig. 8. Examples of $S(0)$ data for water-suspended aggregate objects: (a) colloidal fractal aggregates; (b) black carbon soot; (c) TiO_2 particles just after sonication and (d) after four hours of aggregation. Solid lines in (a) and (b) are the second-order correlation model for fractal aggregates (red), MFA (blue), and granular spheres (green). Solid lines in (c) and (d) are curves obtained from Lorenz–Mie theory, generated using the refractive index $m = n/n_0$ relative to the refractive index of water n_0 (the indices n are reported in each panel). Data in (a) and (b) come from Cremonesi et al. [34], while in (c) and (d) we report previously unpublished supporting data from the same study. Numerical simulations are reported as red crosses (fractals), green circles (granular spheres), and blue discs (MFA model).

221]. This is the most straightforward way to deal with the chemical composition of the particles and obtain their optical properties [72, 128]. To link the scattering signals to the particle properties one needs only two parameters: refractive index and size. In principle, inversion can involve $S(0)$ either particle-by-particle or by first fitting the best *effective* refractive index to data that corresponds to the particle *average* polarizability [145]. It is worth observing that, for particles with small enough ρ so that $K(i\rho)$ can be expanded to the second-order term, $S(0)$ exhibits a very simple behavior in the complex plane. $\Im S(0)$ is proportional to $[\Re S(0)]^{3/4}$, a feature that is better seen by plotting the complex amplitudes in log-scale for populations with size polydispersity at different refractive indices. This indicates whether the MFA can be applied, at least for small ρ. However, the hypothesis of uniform internal distribution and hence the MFA should be questioned if the effective refractive index is much lower than expected.

Real-case particles composed of different materials are rarely mixed uniformly enough to agree with the MFA. Examples are particles where the components are segregated, such as coated particles, fluffy aggregates, and clusters. As introduced in Section 4, $\Re S(0)$ depends on the correlations of the refractive index distribution, or polarization, within the particle: the stronger the correlations, the larger is $\Re S(0)$, and therefore C_{ext}. Once again, measuring $S(0)$ gives insight into this hidden feature of the particle. The second-order expansion reported in Section 4 is applied to colloidal aggregates by Cremonesi et al. [34] as a case study. A detailed description can be given in terms of the structure factor of fractals as there are no free parameters in the model: $S(0)$ is univocally obtained from Eqs. 3,4,(5) and compared with experimental results. Many experiments have been performed with aggregates formed by calibrated, monodisperse polystyrene spheres 70 nm, 100 nm, and 200 nm in diameter. Aggregates have been characterized with independent methods such as SALS and Spectrophotometry.

In Fig. 8, we report some of the results obtained with aggregates compared with the models discussed in Cremonesi et al. [34]. In Fig. 8 (a) we show the results of measurements performed on fractal aggregates formed by well-known, calibrated, monodisperse polystyrene (PS) spheres 100 nm in diameter undergoing a salt-induced aggregation [34]; in (b) the plot shows the results obtained with a water suspension of black carbon soot (BC); we finally show the results of measurements performed on titania white pigment (synthetic TiO_2 powder) suspended in water and strongly sonicated for 30 minutes, then measured immediately (c) and after four hours (d). We point out that all data sets result from merging measurements performed with two instruments with different sensitivities to cover an extended range of the parameters. In (a) we plot the curve describing $S(0)$ for different sizes of the aggregates, obtained without any free parameter (see below for a discussion about the prefactor): we exploit the second-order model reported above for describing fractals (red line), granular spheres (green) and MFA LorenzMie spheres (blue). The difference is striking in terms of $\Re S(0)$, therefore C_{ext}. In (b), the size of the monomers and their complex refractive index are not as well-characterized as in (a). The same three theoretical models (and colors) are reported in b) for fractals built by monomers with a refractive index of 1.85+i0.4 [77]. Data reported in Fig. 8(a) and Fig. 8(b) are compared with the results of numerical simulations from [34] using the ADDA code [236] for fractals and granular spheres (red crosses and green circles, respectively) containing the same number of monomers, as well as the corresponding Lorenz–Mie spheres (blue disks).

In Fig. 8(a) the population of aggregates in the complex $S(0)$ plane shows a deceptively simple yet remarkable feature: $\Im S(0)$ is proportional to $\Re S(0)$. A special feature of fractals is that their density decreases as more monomers are added to the aggregate, therefore, MFA predicts an effective polarizability that decreases with size. However, even taking this into account, extinction is systematically stronger than expected by the MFA model. This trend is incompatible with simply scaling the Rayleigh scattering cross-section with the number of monomers, N. In the second-order model, and from experimental data and simulations, the exponent of $\Re S(0)$ is always 1, whereas in MFA this exponent would depend on the fractal dimension of the aggregate [174,203]. As a result, Eq. (5) provides the correct extinction cross-section but the fractal dimension cannot be obtained from the slope of the $S(0)$population.

In Fig. 8(b), we can appreciate the difference with the dielectric case in (a): data are fitted by models and numerical simulations obtained for fractals, granular spheres, and MFA spheres, and the three are almost indistinguishable. The reason is that absorption dominates extinction ($C_{abs} \sim 6 \cdot C_{sca}$), which can be simply obtained as the number of monomers times the Rayleigh cross-section irrespectively of the mutual positions of the monomers and the orientation of the aggregate. Nevertheless, both in (a) and (b) there is strong evidence of the proportionality with unit power, clearly incompatible with power 3/4 predicted by the Lorenz–Mie model.

As for BC, TiO_2 particles in Fig. 8(c) have monomers that are polydisperse in size: they appear in the lower part of the plot and nicely follow the expected theoretical curve for particles with a refractive index around $n = 2.2$ (red line). Curves are generated using the refractive index $m = n/n_0$ relative to the refractive index of water, n_0, the refractive indices n are reported in the corresponding panels. Particles are reasonably isometric because of their mineralogical structure [109]. Notice that the non-perfect spherical shape induces a slight decrease in the refractive index compared with the expected value, around 2.4 [102, 113]. A second population is evident in the upper part of the data set. It can be fitted by a Lorenz–Mie curve with an effective refractive index $n = 1.56$, suggesting the presence of non-compact objects probably composed of agglomerates of the smaller objects appearing in the lower part of the population. As the system evolves with time, aggregates grow and after four hours the population extends over four decades along both axes (d). Moreover, the whole population does not agree with the unit power law proportionality between $\Im S(0)$ and $\Re S(0)$, suggesting that the TiO_2 aggregates analyzed here are not endowed with a fractal structure. Because of the specific fluidic circuit of the instrument (different from that used for data in (a) and (b)), we cannot guarantee that the shear perturbations induced by the flow through the cell do not modify the structure of the aggregates. Nevertheless, the Lorenz–Mie model with the MFA effective polarizability cannot fit data with a single value of the filling fraction. Towards the largest sizes, in the upper-right region of the plot, the effective refractive index fitted to data down to 1.38 (red line), suggesting the presence of very fluffy structures. Correlations still dominate the particles, although the structure factor is different from that of the fractal aggregates. We can then conclude that in all the cases reported here, the effect of correlations increases $\Re S(0)$ to some degree. This has implications in fields centered on the optical properties of fine powders. Besides the colloidal and soot aggregates mentioned here, assessing the optical properties of aggregates is important for constraining the parameters required by radiative transfer models, with the natural extension to the spectral properties of clouds. Examples can be found in several systems in astrophysics [10,64,86,105, 114,137,197,211] or even in connection with the already mentioned impact of aeolian dust on the Earth's energy balance for climate assessments.

We conclude this section by noticing that fractal models also depend on a parameter that has been the subject of several studies and is still being investigated: the prefactor relating the mass to the ratio between the gyration radius and the monomer radius, to the power of the fractal dimension [74,205]. We point out that the prefactor is a free parameter also in our model, albeit with a minor role. In principle, it can be set by fitting experimental data: changing the prefactor indirectly influences the values of $\Re S(0)$ since it modulates the effect of correlations. Nevertheless, from a practical standpoint, the theoretical curves obtained with prefactor values within the accepted range (1 – 1.35) do not differ enough. Our curves have been then obtained by imposing the prefactor to 1.2, in the middle of its accepted range. Things change in the

case of absorbing aggregates since the range of possible values is much more extended. Anyway, since $\Re\mathrm{e}\ S(0)$ is essentially determined by absorption, which is negligibly influenced by correlations, the value of the prefactor becomes less relevant for absorbing fractals.

8. Measuring more parameters

A further step into this discussion is assessing the angular scattering. For example, one could wonder whether the size of one particle (or the size distribution of a population of particles) obtained from C_{ext} agrees with that obtained from a simultaneous OPC measurement. We achieved that by integrating the scattered fluence within a solid angle around 90° to obtain a parameter that we indicate here as $F(90)$. The method revolves around the single-particle approach. Simultaneous measurements of C_{ext} and $F(90)$ take advantage of the continuous monitoring of the incident beam power, which is intrinsically self-referenced. $F(90)$ can then be calibrated with known particles and matched with the forward scattering, thus providing a complete set of data for each particle. If the complex $S(0)$ is measured, inversions from $\Im\mathrm{m}\ S(0)$ and $F(0)$ can also be obtained and compared with those from $F(90)$. Possible discrepancies are a fingerprint of a deviation from the ideal spherical approximation.

Let $F(\Theta)$ be the integral of the fluence over a given solid angle around the scattering angle Θ. We recall that the ratio between the integral $F(\Theta)$ and the total *scattering* cross-section, C_{sca}, is by definition the phase factor multiplied by k^2. By introducing the single scattering albedo $ssa = C_{\mathrm{sca}}/C_{\mathrm{ext}}$ we find:

$$ssa \cdot p(\Theta) = F(\Theta)/C_{\mathrm{ext}} \tag{6}$$

The ratio on the left can be also given by the ratio of the photocurrents from the corresponding sensors, provided that the electronics and the acquisition are identical in the two measurements. Therefore, the result is independent of any geometrical or experimental parameter [32] except for *ssa*. This cannot be measured simultaneously with the other parameters appearing in Eq. (9) and is not trivial [134] as it is equivalent to being able to resolve the contributions of C_{sca} and C_{abs}. Nevertheless, especially when aiming at measuring $p(\Theta)$ for radiative transfer applications, one can rely on estimates, even derived from $S(0)$ itself. Moreover, an additional constraint exists because of the normalization of the function $p(\Theta)$. Notice that in case $S(0)$ is measured, $F(0)$ represents an additional, significant constraint to the integral. The importance of single-particle measurements to assess these results is clear.

Here we report an example of simultaneous measurements of $S(0)$ and $F(\Theta)$ of airborne dust, performed through a modified SPES instrument including an additional sensor collecting scattered light within a wide solid angle around 90° [32]. The instrument is permanently installed and operating in Antarctica, Concordia Station at DomeC, the cleanest place in the world, to assess optical properties of aeolian dust transported mainly from the Southern hemisphere deserts. The instrument is operated within the project OPTAIR, funded by the Italian Antarctic Program. We show data from 2019 as two-dimensional histograms: Fig. 9(a) the complex plane for $S(0)$ and Fig. 9(b) a plot of the $F(0)$ (blue–green) and $F(90)$ (red–yellow) raw data plotted against C_{ext}.

In Fig. 9(c), (d), and (e), we report the size distributions obtained

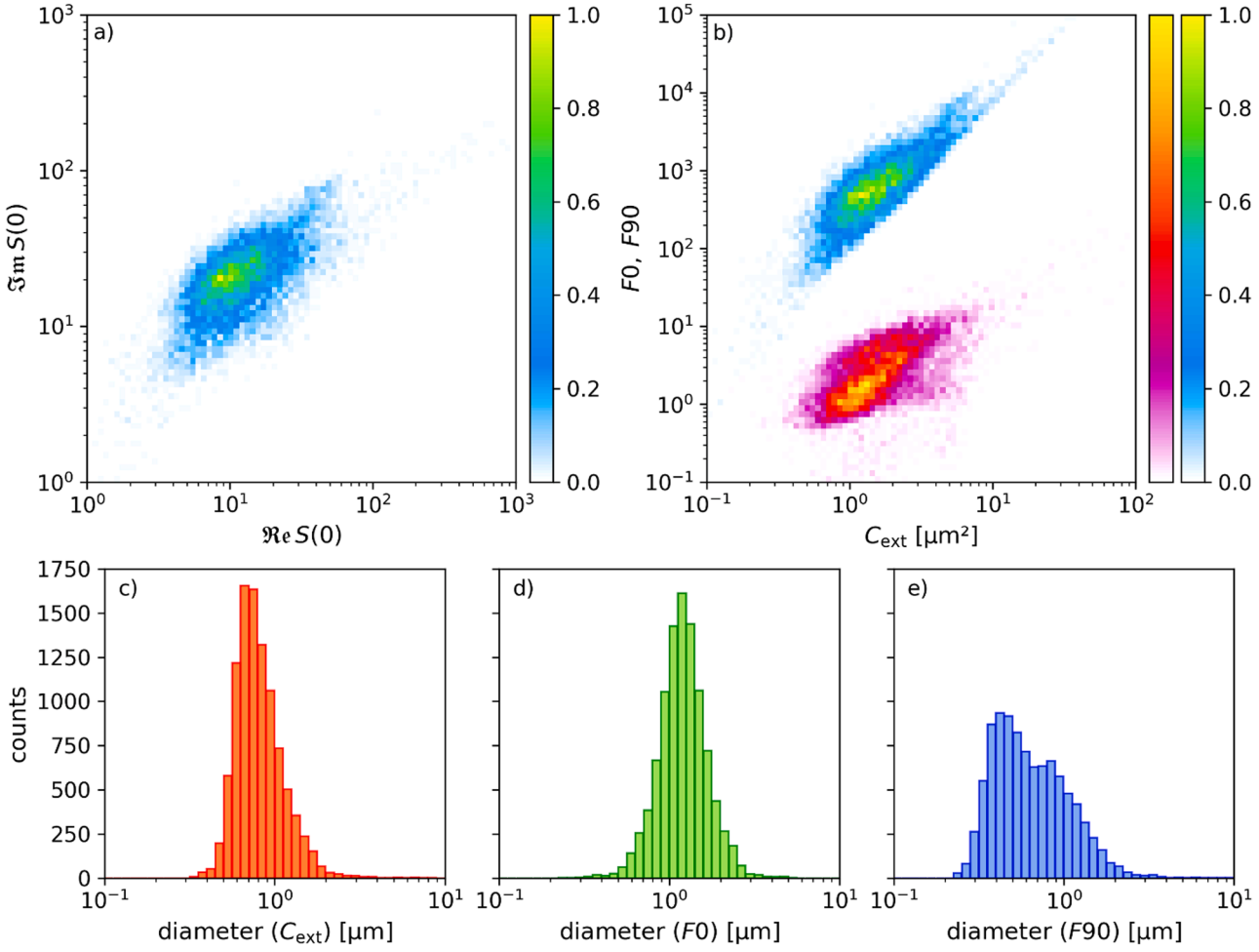

Fig. 9. Data from airborne dust representing $S(0)$ (a), $F(0)$, and $F(90)$ as a function of C_{ext} (b) and three size distributions obtained from the values of C_{ext}, $F(0)$ and $F(90)$ in panels (c), (d), and (e), respectively. Data from an unpublished dataset from the study by Cremonesi et al. [35].

from C_{ext}, $F(0)$, and $F(90)$, respectively. We invert data using monotonic functions best fitted to the Lorenz–Mie curves for spheres with refractive index in the range of the mineral species under consideration, $n = 1.55 + i0.005$. As expected, the inversion provides the same results if we restrict the dataset to spherical particles (not shown), while the results are remarkably different in general (panels c–d of Fig. 9). The relevant discrepancies indicate appreciable deviations from the ideal Lorenz–Mie model. Qualitative and quantitative differences are evident: the size distributions show median sizes of 0.88 μm, 1.13 μm, and 0.75 μm, with a discrepancy of 50% between the maximum and minimum values. Comparing statistical parameters like the geometric standard deviation (describing lognormal distributions) gives 1.39 μm, 1.38 μm, and 1.66 μm. Finally, we notice an apparent asymmetry and skewness in the size distribution obtained from $F(90)$, which is, in fact, bimodal, while the other two appear much more symmetric.

Characterizing $F(90)$ gives insight into the optical properties of inhomogeneous particles [35]. Here we report the results of a variety of measurements performed on the same samples used to generate the experimental results reported in Fig. 8(a) and (b), namely PS spheres and BC soot. As in Fig. 8, numerical simulations are performed on model aggregates and simplified analytical models, as described below. Data in Fig. 8(a) come from an over-constrained system where the main factor is the correlation function, or its Fourier transform. The same numerical results reported in Fig. 8(a) allow us to extract the corresponding values for $F(90)$, integrated over the same solid angle adopted in the optical device described above. Results are reported in Fig. 10(a), where red, green, and blue points represent fractals, granular spheres, and MFA spheres, respectively. Lines with the corresponding colors describe the results of the analytical or semi-analytical models, following the method described in Sorensen er al. [208] for the fractals and granular spheres while we adopted the Lorenz–Mie model for the MFA spheres. The plots show two main results: i) the discrepancy between the fractal aggregates and the corresponding MFA spheres, reaching orders of magnitude at the largest sizes; ii) the superposition of the fractals and the granular spheres due to scattering at large angles by the small monomers, which are identical in the two cases. Notice that, on the contrary, the corresponding values in the $S(0)$ complex plane (Fig. 10(a)) are separated due to the influence of correlations, as observed above. Therefore, inverting to size from C_{ext} and $F(90)$ will give considerably different results. In Fig. 10(b), a similar plot is reported for the BC soot. The detection threshold of the device used to collect the data has appreciably limited the result, nevertheless, panel (b) supports the key point as in (a). Numerical and semi-analytical results have been obtained by fitting the necessary parameters to the data reported in Fig. 8(b). A similar discrepancy observed in (a) is found here between the experimental results and the MFA model. Moreover, we stress that this result provides an additional insight of utmost importance in terms of the *ssa*: if estimated with the MFA model, the result would be wrong; assuming the complex polarizability of the aggregate to be that of the bulk material would be worse. Inverting $F(90)$ would not give the correct size and in lack of independent measurements one can hardly be aware of this. Conversely, the measure of $S(0)$ brings enough information to highlight the correlations within the particles, suggesting how to evaluate, even roughly and with simple models, the behavior of $p(90)$ and more generally $p(\vartheta)$.

9. Discussion and perspectives

The phase shift parameter ρ can be identified as a key to determining the overall behavior of the internal fields within the particle volume. The diffraction of these fields plays the role of the scattering pattern in the far field, therefore, scattering data embed precious information about ρ [92,202]. This is not related to just one observable: recovering ρ would first require inverting the parameters of the particle by which is defined and addressing the connected issues. Nevertheless, ρ ultimately determines the complex amplitude $S(0)$, albeit for a generic particle. Moreover, as discovered by Sorensen [92,202], and preliminary evidenced by the approximated homologous scattering diagrams (see Fig. 2), ρ is linked to the small-angle scattering pattern if scaled in terms of the dimensionless wavevector qa. An example of this is the regularity of the pattern of maxima and minima, as highlighted in Fig. 2. We also draw attention to the relatively uniform $A(\rho, qa)$ despite the wide range of the unnormalized $|S(\rho, qa)|$ values over such a range of parameters. By extending to more general cases, Lorenz–Mie scattering can be cast in a similar expression [204], paving the way for new visions on light scattering. Besides the theoretical interest, such a result can be relevant in assessing the scattering features of particles in the intermediate size range, which is still lacking viable approaches [187]. Moreover, merging the results by Sorensen with measurements of $S(0)$ gives a new way of characterizing the optical properties of particles in real environments.

We have reported a recent result obtained by Parola et al. [160] that includes the radiation reaction term in the second-order expansion of $S(0)$, elucidating the role of the statistical inhomogeneities of the internal fields with a relation between the forward-scattered field and the

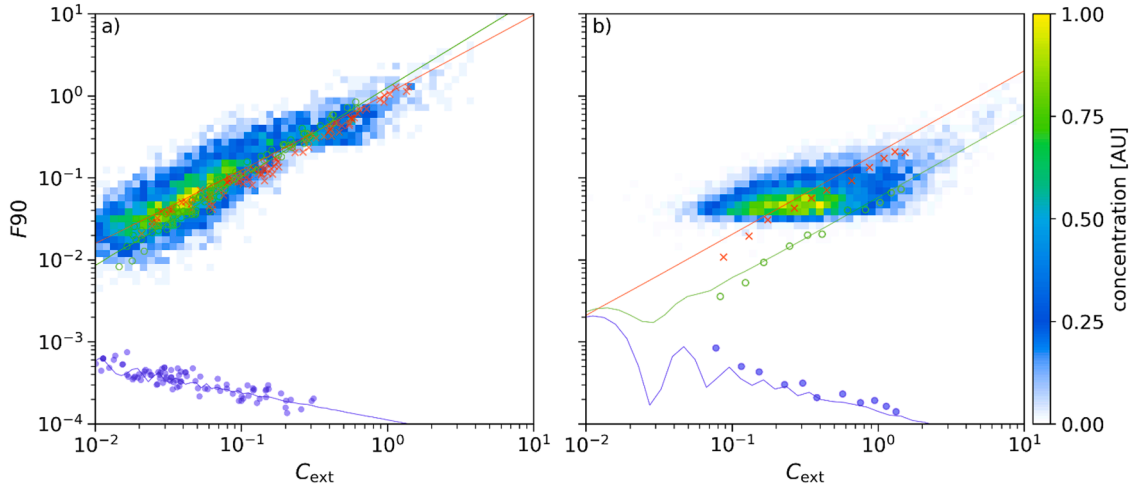

Fig. 10. Measurements of $F(90)$ plotted vs C_{ext} for the samples reported in Fig. 8(a) (fractals) and (b) (BC soot). Red crosses, green circles, and blue discs represent the results of numerical computation for fractals, granular spheres, and Lorenz–Mie (MFA) models respectively. Solid lines represent the curves from analytical or semi-analytical models: red, green, and blue indicate fractals, granular spheres, and Lorenz–Mie theoretical expectations, respectively. Notice the discrepancy between the experimental results (and the corresponding models) and the expectations from MFA. Data from Cremonesi et al. [34].

scattering pattern. Such relation is based on the Fourier transform, one of the fundamentals of scattering, and is an experimental check of the optical theorem. What emerges from the examples of non-spherical particles, aggregates, and absorbing particles reported in the previous sections is that measuring two parameters is enough to assess the validity of models from experimental data.

We stress the importance of going beyond sizing from scattering measurements. While it is more natural to think in terms of size distributions, theory and experiments are both affected by the difficulties of approaching inverse problems. For many applications, this is not a strict requirement but rather a discretionary intermediate step that introduces unbound errors at the expense of more relevant parameters. Especially for particles endowed with complex morphology, sizing needs a shift of attention towards other properties that may be determined unambiguously and a convenient definition of "size". As an example, the distribution of the extinction cross-section is relevant in its own right for assessing the radiative budget of multi-corpuscles systems. Moreover, C_{ext} can be measured from both simple obscuration and $S(0)$ and it is less affected by the particle characteristics. Conversely, it depends on the radiation wavelength, with a substantial impact on the spectral features [34]. This concerns any collection of absorbing objects, wavelength-dependent optical properties, or internal mixing, to cite some examples where the contribution of scattering can appreciably change the spectral attenuation of light, the spectral dependence of *ssa*, the scattering cross-sections and their angular dependence. Handling size distributions, even when the composition is known, can hide the actual radiative properties of the object or system under study, as already known by the scientific community [47,103,122,147].

In perspective, finding general rules to estimate the optical properties of mineral dust and carbonaceous particles will help to quantitatively address a wide class of problems related to climate change: radiative transfer and dust behavior in the atmosphere, dust transport and temporal evolution, snow albedo in presence of wet or dry dust deposition, etc. [78,84,237]. The development of dedicated numerical approaches to describe light scattering from particles and innovative approaches for radiative transfer computation will likely characterize the years to come (see [209] and references therein). Nevertheless, following the European Union indications to tackle climate change, the assessment of stronger experimental approaches, as well as accurate and widespread environmental monitoring, will be the next step forward that will contribute to validating models, putting constraints, and providing data from model samples that will be merged with the numerical results to constrain models and fit the observation. The extending suite of ground-based monitoring stations and Earth observation satellites being currently implemented will provide unprecedented data, that will require powerful interpretation models [51,153].

Declaration of Competing Interest

The authors declare the following financial interests/personal relationships which may be considered as potential competing interests: Marco A.C. Potenza reports a relationship with EOS that includes board membership and equity or stocks. Marco A.C. Potenza has patented *Giglio M, Potenza MAC. A method of measuring properties of particles and corresponding apparatus* (Patent No: WO2006137090A1) owned by the University of Milan and licensed to EOS S.r.l.

Data availability

Data will be made available on request.

Acknowledgments

The authors acknowledge Marzio Giglio for more than a decade of discussions about light scattering, Tiziano Sanvito and Marco Pallavera of EOS S.r.l. for lending one of the instruments and the corresponding technical support, and the Italian National Antarctic Research Program (PNRA): this paper is a contribution to the PNRA16_00231 project "OPTAIR" and to the PNRA18_00058 project "ICE-OPT".

References

[1] Albanese A, Tang PS, Chan WC. The effect of nanoparticle size, shape, and surface chemistry on biological systems. Annu Rev Biomed Eng 2012;14:1–16.
[2] Albani S, Mahowald N, Perry A, Scanza R, Zender C, Heavens N, Maggi V, Kok J, Otto-Bliesner B. Improved dust representation in the Community Atmosphere Model. J Adv Model Earth Syst 2014;6:541–70.
[3] Anderson T, Covert D, Wheeler J, Harris J, Perry K, Trost B, Jaffe D, Ogren J. Aerosol backscatter fraction and single scattering albedo: measured values and uncertainties at a coastal station in the Pacific Northwest. J Geophys Res Atmos 1999;104:26793–807.
[4] Anderson TL, Ogren JA. Determining aerosol radiative properties using the TSI 3563 integrating nephelometer. Aerosol Sci Technol 1998;29:57–69.
[5] Aptowicz KB, Chang RK. Angularly-resolved elastic scatter from single particles collected over a large solid angle and with high resolution. J Phys: Conf Ser IOP Publish 2005. 006.
[6] Aptowicz KB, Pan Y-L, Martin SD, Fernández E, Chang RK, Pinnick RG. Decomposition of atmospheric aerosol phase function by particle size and asphericity from measurements of single particle optical scattering patterns. J Quant Spectrosc Radiat Transf 2013;131:13–23.
[7] Bassini A, Menchise M, Musazzi S, Paganini E, Perini U. Interferometric system for precise submicrometer particle sizing. Appl Opt 1997;36:8121–7.
[8] Batchelder J, Taubenblatt M. Interferometric detection of forward scattered light from small particles. Appl Phys Lett 1989;55:215–7.
[9] Batchelder, J.S., Taubenblatt, M.A., 1990. Measurement of size and refractive index of particles using the complex forward-scattered electromagnetic field.
[10] Bazell D, Dwek E. The effects of compositional inhomogeneities and fractal dimension on the optical properties of astrophysical dust. Astrophys J 1990;360:142–50.
[11] Berg M, Sorensen CM, Chakrabarti A. Explanation of the patterns in Mie theory. J Quant Spectrosc Radiat Transf 2010;111:782–94.
[12] Berg MJ, Holler S. Simultaneous holographic imaging and light-scattering pattern measurement of individual microparticles. Opt Lett 2016;41:3363–6.
[13] Berg MJ, Sorensen CM, Chakrabarti A. Extinction and the optical theorem. Part I. Single particles. JOSA A 2008;25:1504–13.
[14] Berg MJ, Sorensen CM, Chakrabarti A. Patterns in Mie scattering: evolution when normalized by the Rayleigh cross section. Appl Opt 2005;44:7487–93.
[15] Berg MJ, Videen G. Digital holographic imaging of aerosol particles in flight. J Quant Spectrosc Radiat Transf 2011;112:1776–83.
[16] Berne BJ, Pecora R. Dynamic light scattering: with applications to chemistry, biology, and physics. Dover Publications; 2000.
[17] Bickel WS, Gilliar W, Bell B. Light scattering from fibers: a closer look with a new twist. Appl Opt 1980;19:3671–5. https://doi.org/10.1364/AO.19.003671.
[18] Bohren CF. Atmospheric Optics. Digital encyclopedia of applied physics. John Wiley & Sons, Ltd; 2005. https://doi.org/10.1002/3527600434.eap295.pub2.
[19] Bohren CF, Huffman DR. Absorption and scattering of light by small particles. John Wiley & Sons; 1983.
[20] Borghese F, Denti P, Saija R. Scattering from model nonspherical particles: theory and applications to environmental physics. Springer Science & Business Media; 2007.
[21] Born M, Wolf E. Principles of Optics, 7th (expanded) edition. U K Press Synd Univ Camb 1999;461:401–24.
[22] Carr Jr ME, Hermans J. Size and density of fibrin fibers from turbidity. Macromolecules 1978;11:46–50.
[23] Ceolato R, Berg MJ. Aerosol light extinction and backscattering: a review with a lidar perspective. J Quant Spectrosc Radiat Transf 2021;262:107492.
[24] Chandrasekhar, S., 2013. Radiative transfer. Courier Corporation.
[25] Charrière F, Marian A, Montfort F, Kuehn J, Colomb T, Cuche E, Marquet P, Depeursinge C. Cell refractive index tomography by digital holographic microscopy. Opt Lett 2006;31:178–80.
[26] Chesler A, Winski D, Kreutz K, Koffman B, Osterberg E, Ferris D, Thundercloud Z, Mohan J, Cole-Dai J, Wells M, Handley M, Putnam A, Anderson K, Harmon N. Non-spherical microparticle shape in Antarctica during the last glacial period affects dust volume-related metrics. Clim Past 2023;19:477–92. https://doi.org/10.5194/cp-19-477-2023.
[27] Chu B, Liu T. Characterization of nanoparticles by scattering techniques. J Nanoparticle Res 2000;2:29–41.
[28] Chỳlek P, Grams G, Pinnick R. Light scattering by irregular randomly oriented particles. Science 1976;193:480–2.
[29] Chỳlek P, Klett JD. Extinction cross sections of nonspherical particles in the anomalous diffraction approximation. JOSA A 1991;8:274–81.
[30] Chỳlek P, Srivastava V, Pinnick RG, Wang R. Scattering of electromagnetic waves by composite spherical particles: experiment and effective medium approximations. Appl Opt 1988;27:2396–404.
[31] Cipelletti L, Bissig H, Trappe V, Ballesta P, Mazoyer S. Time-resolved correlation: a new tool for studying temporally heterogeneous dynamics. J Phys Condens Matter 2003;15:S257. https://doi.org/10.1088/0953-8984/15/1/334.
[32] Cornillault J. Particle size analyzer. Appl Opt 1972;11:265–8.

[33] Cotterell MI, Knight JW, Reid JP, Orr-Ewing AJ. Accurate Measurement of the Optical Properties of Single Aerosol Particles Using Cavity Ring-Down Spectroscopy. J Phys Chem A 2022;126:2619–31. https://doi.org/10.1021/acs.jpca.2c01246.
[34] Cremonesi L, Minnai C, Ferri F, Parola A, Paroli B, Sanvito T, Potenza MA. Light extinction and scattering from aggregates composed of submicron particles. J Nanoparticle Res 2020;22:1–17.
[35] Cremonesi L, Passerini A, Tettamanti A, Paroli B, Delmonte B, Albani S, Cavaliere F, Viganò D, Bettega G, Sanvito T. Multiparametric optical characterization of airborne dust with single particle extinction and scattering. Aerosol Sci Technol 2020;54:353–66.
[36] Cremonesi L, Siano M, Paroli B, Potenza MA. Near field scattering for samples under forced flow. Rev Sci Instrum 2020;91:075108.
[37] Cuche E, Bevilacqua F, Depeursinge C. Digital holography for quantitative phase-contrast imaging. Opt Lett 1999;24:291–3.
[38] Cuche E, Marquet P, Depeursinge C. Simultaneous amplitude-contrast and quantitative phase-contrast microscopy by numerical reconstruction of Fresnel off-axis holograms. Appl Opt 1999;38:6994–7001.
[39] Debye P. The diffraction theory of aberrations. Ann Phys Leipzig 1909;30:59–62.
[40] Degiorgio V, Bellini T, Piazza R, Mantegazza F. Forward depolarized light scattering: heterodyne versus homodyne detection. Phys Stat Mech Appl 1997;235:279–90.
[41] Degiorgio V, Piazza R, Bellini T. Static and dynamic light scattering study of fluorinated polymer colloids with a crystalline internal structure. Adv Colloid Interface Sci 1994;48:61–91.
[42] Degiorgio V, Potenza MA, Giglio M. Scattering from anisotropic particles: a challenge for the optical theorem? Eur Phys J E 2009;29:379–82.
[43] Delmonte B, Petit JR, Krinner G, Maggi V, Jouzel J, Udisti R. Ice core evidence for secular variability and 200-year dipolar oscillations in atmospheric circulation over East Antarctica during the Holocene. Clim Dyn 2005;24:641–54.
[44] Dick WD, Ziemann PJ, Huang P-F, McMurry PH. Optical shape fraction measurements of submicrometre laboratory and atmospheric aerosols. Meas Sci Technol 1998;9:183.
[45] Djorovic A, Oldenburg SJ, Grand J, Le Ru EC. Extinction-to-absorption ratio for sensitive determination of the size and dielectric function of gold nanoparticles. ACS Nano 2020;14:17597–605.
[46] Doicu A, Wriedt T, Khebbache N. An overview of the methods for deriving recurrence relations for T-matrix calculation. J Quant Spectrosc Radiat Transf 2019;224:289–302.
[47] Doner N, Liu F. Impact of morphology on the radiative properties of fractal soot aggregates. J Quant Spectrosc Radiat Transf 2017;187:10–9. https://doi.org/10.1016/j.jqsrt.2016.09.005.
[48] Draine BT. Interstellar dust grains. Annu Rev Astron Astrophys 2003;41:241–89.
[49] Draine BT, Flatau PJ. Discrete-dipole approximation for scattering calculations. Josa A 1994;11:1491–9.
[50] Drossart P. A statistical model for the scattering by irregular particles. Astrophys J 1990;361:L29–32.
[51] Dubovik O, Fuertes D, Litvinov P, Lopatin A, Lapyonok T, Doubovik I, Xu F, Ducos F, Chen C, Torres B. A comprehensive description of multi-term LSM for applying multiple a priori constraints in problems of atmospheric remote sensing: GRASP algorithm, concept, and applications. Front Remote Sens 2021;2:706851. Doi 103389frsen.
[52] Dubovik O, Holben B, Eck TF, Smirnov A, Kaufman YJ, King MD, Tanré D, Slutsker I. Variability of absorption and optical properties of key aerosol types observed in worldwide locations. J Atmospheric Sci 2002;59:590–608.
[53] Dubovik O, Sinyuk A, Lapyonok T, Holben BN, Mishchenko M, Yang P, Eck TF, Volten H, Muñoz O, Veihelmann B. Application of spheroid models to account for aerosol particle nonsphericity in remote sensing of desert dust. J Geophys Res Atmos 2006;111.
[54] Eidhammer T, Montague DC, Deshler T. Determination of index of refraction and size of supermicrometer particles from light scattering measurements at two angles. J Geophys Res Atmos 2008;113.
[55] Einstein A. Theorie der opaleszenz von homogenen flüssigkeiten und flüssigkeitsgemischen in der nähe des kritischen zustandes. Ann Phys 1910;338:1275–98.
[56] Emde C, Buras-Schnell R, Kylling A, Mayer B, Gasteiger J, Hamann U, Kylling J, Richter B, Pause C, Dowling T. The libRadtran software package for radiative transfer calculations (version 2.0. 1). Geosci Model Dev 2016;9:1647–72.
[57] Fernández-Barbero A, Schmitt A, Cabrerizo-Vílchez M, Martínez-García R. Cluster-size distribution in colloidal aggregation monitored by single-cluster light scattering. Phys Stat Mech Appl 1996;230:53–74.
[58] Fernandez-Barbero A, Schmitt A, Cabrerizo-Vilchez M, Martínez-García R, Hidalgo-Alvarez R. Influence of cluster morphology on calculation of the aggregation rate constant in mesoscopic systems. Phys Rev E 1997;56:4337.
[59] Ferri F. Use of a charge coupled device camera for low-angle elastic light scattering. Rev Sci Instrum 1997;68:2265–74.
[60] Ferri F, Bassini A, Paganini E. Commercial spectrophotometer for particle sizing. Appl Opt 1997;36:885–91.
[61] Ferri F, Calegari GR, Molteni M, Cardinali B, Magatti D, Rocco M. Size and density of fibers in fibrin and other filamentous networks from turbidimetry: beyond a revisited Carr–Hermans method, accounting for fractality and porosity. Macromolecules 2015;48:5423–32.
[62] Ferri F, Giglio M, Paganini E, Perini U. Low-angle elastic light scattering study of diffusion-limited aggregation. EPL Europhys Lett 1988;7:599–604.
[63] Ferri F, Giglio M, Perini U. Inversion of light scattering data from fractals by the Chahine iterative algorithm. Appl Opt 1989;28:3074–82.
[64] Fogel ME, Leung CM. Modeling extinction and infrared emission from fractal dust grains: fractal dimension as a shape parameter. Astrophys J 1998;501:175.
[65] Forster P. Climate change 2021: the physical science basis. contribution of working group I to the sixth assessment report of the intergovernmental panel on climate change. Cambridge, United Kingdom and New York, USA: Cambridge University Press; 2021.
[66] Frisken BJ. Revisiting the method of cumulants for the analysis of dynamic light-scattering data. Appl Opt 2001;40:4087–91.
[67] Fu R, Wang C, Muñoz O, Videen G, Santarpia JL, Pan Y-L. Elastic back-scattering patterns via particle surface roughness and orientation from single trapped airborne aerosol particles. J Quant Spectrosc Radiat Transf 2017;187:224–31.
[68] Garcia-Sucerquia J, Xu W, Jericho SK, Klages P, Jericho MH, Kreuzer HJ. Digital in-line holographic microscopy. Appl Opt 2006;45:836–50.
[69] Garner, R., 2022. NASA's Webb reveals steamy atmosphere of distant planet in detail [WWW Document]. NASA. URL http://www.nasa.gov/image-feature/goddard/2022/nasa-s-webb-reveals-steamy-atmosphere-of-distant-planet-in-detail (accessed 3.28.23).
[70] Gasteiger J, Wiegner M, Groß S, Freudenthaler V, Toledano C, Tesche M, Kandler K. Modelling lidar-relevant optical properties of complex mineral dust aerosols. Tellus B Chem Phys Meteorol 2011;63:725–41.
[71] Gebhart J. Response of single-particle optical counters to particles of irregular shape. Part Part Syst Charact 1991;8:40–7.
[72] Ghan SJ, Zaveri RA. Parameterization of optical properties for hydrated internally mixed aerosol. J Geophys Res Atmos 2007;112.
[73] Giglio, M., Potenza, M.A., 2011. Method of measuring properties of particles and corresponding apparatus.
[74] Gmachowski L. Calculation of the fractal dimension of aggregates. Colloids Surf Physicochem Eng Asp 2002;211:197–203.
[75] Gong Z, Pan Y-L, Wang C. Characterization of single airborne particle extinction using the tunable optical trap-cavity ringdown spectroscopy (OT-CRDS) in the UV. Opt Express 2017;25:6732–45.
[76] Grand J, Auguieé B, Le Ru EC. Combined extinction and absorption UV–visible spectroscopy as a method for revealing shape imperfections of metallic nanoparticles. Anal Chem 2019;91:14639–48.
[77] Gravatt C. The applications of light scattering. Appl Spectrosc 1971;25:509–16.
[78] Hansen J, Nazarenko L. Soot climate forcing via snow and ice albedos. Proc Natl Acad Sci 2004;101:423–8. https://doi.org/10.1073/pnas.2237157100.
[79] Hansen JE, Cheyney H. Near infrared reflectivity of venus and ice clouds. J Atmospheric Sci 1968;25:629–33. 10.1175/1520-0469(1968)025<0629:NIROVA>2.0.CO;2.
[80] Hansen JE, Lacis AA. Sun and dust versus greenhouse gases: an assessment of their relative roles in global climate change. Nature 1990;346:713–9.
[81] Harvey L. Climatic impact of ice-age aerosols. Nature 1988;334:333–5.
[82] Heim M, Mullins BJ, Umhauer H, Kasper G. Performance evaluation of three optical particle counters with an efficient "multimodal" calibration method. J Aerosol Sci 2008;39:1019–31.
[83] Heinson WR, Chakrabarti A, Sorensen CM. A new parameter to describe light scattering by an arbitrary sphere. Opt Commun 2015;356:612–5.
[84] Heinson YW, Maughan JB, Heinson WR, Chakrabarti A, Sorensen CM. Light scattering Q-space analysis of irregularly shaped particles. J Geophys Res Atmospheres 2016;121:682–91. https://doi.org/10.1002/2015JD024171.
[85] Heintzenberg J, Charlson RJ. Design and applications of the integrating nephelometer: a review. J Atmospheric Ocean Technol 1996;13:987–1000.
[86] Henning T, Stognienko R. Dust opacities for protoplanetary accretion disks: influence of dust aggregates. Astron Astrophys 1996;311:291–303.
[87] Hoekstra A, Grimminck M, Sloot P. Large scale simulations of elastic light scattering by a fast discrete dipole approximation. Int J Mod Phys C 1998;9:87–102.
[88] Hoekstra AG, Sloot PM. New computational techniques to simulate Light Scattering from arbitrary particles. Part Part Syst Charact 1994;11:189–93.
[89] Holben BN, Eck T, Slutsker Ial, Tanre D, Buis J, Setzer A, Vermote E, Reagan JA, Kaufman Y, Nakajima T. AERONET—A federated instrument network and data archive for aerosol characterization. Remote Sens Environ 1998;66:1–16.
[90] Holler S, Pan Y, Chang RK, Bottiger JR, Hill SC, Hillis DB. Two-dimensional angular optical scattering for the characterization of airborne microparticles. Opt Lett 1998;23:1489–91.
[91] Holler S, Zomer S, Crosta GF, Chang RK, Bottiger JR. Multivariate analysis and classification of two-dimensional angular optical scattering patterns from aggregates. Appl Opt 2004;43:6198–206.
[92] Hubbard J, Eckels S, Sorensen CM. Q-space analysis applied to polydisperse, dense random aggregates. Part Part Syst Charact 2008;25:68–73.
[93] Hunt AJ, Huffman DR. A new polarization-modulated light scattering instrument. Rev Sci Instrum 2003;44:1753–62. https://doi.org/10.1063/1.1686049.
[94] Ignatovich FV, Novotny L. Real-time and background-free detection of nanoscale particles. Phys Rev Lett 2006;96:013901.
[95] ISO21501-1. Determination of particle size distribution – Single particle light interaction methods – Light scattering aerosol spectrometer (Standard No. ISO21501-1). Int Org Standard 2009. Geneva, CH.
[96] ISO21501-3. Determination of particle size distribution – Single particle light interaction methods – Light extinction liquid-borne particle counter (Standard No. ISO21501-3). Int Org Standard, Geneva, CH 2019.
[97] ISO21501-4. Determination of particle size distribution – Single particle light interaction methods – Light scattering airborne particle counter for clean spaces (Standard No. ISO21501-4). Int Org Standard, Geneva, CH 2018.

[98] Jakubczyk T, Jakubczyk D, Stachurski A. Assessing the properties of a colloidal suspension with the aid of deep learning. J Quant Spectrosc Radiat Transf 2021; 261:107496. https://doi.org/10.1016/j.jqsrt.2020.107496.

[99] Jeffery GB. The motion of ellipsoidal particles immersed in a viscous fluid. Proc R Soc Lond Ser Contain Pap Math Phys Character 1922;102:161–79.

[100] Jin J-M. The finite element method in electromagnetics. John Wiley & Sons; 2015.

[101] Johnson BR. Invariant imbedding T matrix approach to electromagnetic scattering. Appl Opt 1988;27:4861–73. https://doi.org/10.1364/AO.27.004861.

[102] Jolivet A, Labbé C, Frilay C, Debieu O, Marie P, Horcholle B, Lemarié F, Portier X, Grygiel C, Duprey S, Jadwisienczak W, Ingram D, Upadhyay M, David A, Fouchet A, Lüders U, Cardin J. Structural, optical, and electrical properties of TiO2 thin films deposited by ALD: impact of the substrate, the deposited thickness and the deposition temperature. Appl Surf Sci 2023;608:155214. https://doi.org/10.1016/j.apsusc.2022.155214.

[103] Kahnert M. On the discrepancy between modeled and measured mass absorption cross sections of light absorbing carbon aerosols. Aerosol Sci Technol 2010;44: 453–60. https://doi.org/10.1080/02786821003733834.

[104] Kahnert M, Nousiainen T, Lindqvist H. Model particles in atmospheric optics. J Quant Spectrosc Radiat Transf 2014;146:41–58.

[105] Kataoka A, Okuzumi S, Tanaka H, Nomura H. Opacity of fluffy dust aggregates. Astron Astrophys 2014;568:A42.

[106] Kaye PH, Hirst E, Clark J, Micheli F. Airborne particle shape and size classification from spatial light scattering profiles. J Aerosol Sci 1992;23: 597–611.

[107] Keller AA, McFerran S, Lazareva A, Suh S. Global life cycle releases of engineered nanomaterials. J Nanoparticle Res 2013;15:1–17.

[108] Kemppinen O, Nousiainen T, Lindqvist H. The impact of surface roughness on scattering by realistically shaped wavelength-scale dust particles. J Quant Spectrosc Radiat Transf 2015;150:55–67.

[109] Kemppinen O, Nousiainen T, Merikallio S, Räisänen P. Retrieving microphysical properties of dust-like particles using ellipsoids: the case of refractive index. Atmospheric Chem Phys 2015;15:11117–32.

[110] Kerker M, Farone W, Smith L, Matijević E. Determination of particle size by the minima and maxima in the angular dependence of the scattered light. Range of validity of the method. J Colloid Sci 1964;19:193–200.

[111] Khadir S, Andrén D, Chaumet PC, Monneret S, Bonod N, Käll M, Sentenac A, Baffou G. Full optical characterization of single nanoparticles using quantitative phase imaging. Optica 2020;7:243–8.

[112] Kim MK. Principles and techniques of digital holographic microscopy. SPIE Rev 2010;1:018005.

[113] Koleske, 1995. Paint and coating testing manual : fourteenth edition of the Gardner - Sward handbook.

[114] Kozasa T, Blum J, Mukai T. Optical properties of dust aggregates: I. Wavelength dependence. Astron Astrophys 1992;263:423–32.

[115] Landau LD, Bell J, Kearsley M, Pitaevskii L, Lifshitz E, Sykes J. Electrodynamics of continuous media. elsevier; 2013.

[116] Lane P, Hart M, Jain V, Tucker J, Eversole J. Characterization of single particle aerosols by elastic light scattering at multiple wavelengths. J Quant Spectrosc Radiat Transf 2018;208:188–95.

[117] Lefevre M, Oumbe A, Blanc P, Espinar B, Gschwind B, Qu Z, Wald L, Schroedter-Homscheidt M, Hoyer-Klick C, Arola A. McClear: a new model estimating downwelling solar radiation at ground level in clear-sky conditions. Atmospheric Meas Tech 2013;6:2403–18.

[118] Li C, Kattawar GW, Yang P. Identification of aerosols by their backscattered Mueller images. Opt Express 2006;14:3616–21.

[119] Liebling M, Blu T, Unser M. Complex-wave retrieval from a single off-axis hologram. JOSA A 2004;21:367–77.

[120] Lin M, Lindsay H, Weitz D, Ball R, Klein R, Meakin P. Universal reaction-limited colloid aggregation. Phys Rev A 1990;41:2005.

[121] Lin M, Lindsay H, Weitz D, Ball R, Klein R, Meakin P. Universality in colloid aggregation. Nature 1989;339:360–2.

[122] Liu C, Teng S, Zhu Y, Yurkin MA, Yung YL. Performance of the discrete dipole approximation for optical properties of black carbon aggregates. J Quant Spectrosc Radiat Transf 2018;221:98–109. https://doi.org/10.1016/j.jqsrt.2018.09.030.

[123] Liu Y, Daum PH. The effect of refractive index on size distributions and light scattering coefficients derived from optical particle counters. J Aerosol Sci 2000; 31:945–57.

[124] Macke A, Mueller J, Raschke E. Single scattering properties of atmospheric ice crystals. J Atmospheric Sci 1996;53:2813–25.

[125] Mahowald N, Albani S, Kok JF, Engelstaeder S, Scanza R, Ward DS, Flanner MG. The size distribution of desert dust aerosols and its impact on the Earth system. Aeolian Res 2014;15:53–71.

[126] Mandelstam L. Über optisch homogene und trübe Medien. Ann Phys 1907;328: 626–42.

[127] Mariani F, Bernardoni V, Riccobono F, Vecchi R, Valli G, Sanvito T, Paroli B, Pullia A, Potenza MA. Single particle extinction and scattering allows novel optical characterization of aerosols. J Nanoparticle Res 2017;19:1–15.

[128] Markel VA. Introduction to the Maxwell Garnett approximation: tutorial. JOSA A 2016;33:1244–56.

[129] Maron SH, Elder ME. Determination of latex particle size by light scattering. I. Minimum intensity method. J Colloid Sci 1963;18:107–18.

[130] Martín JCG, Guirado D, Frattin E, Bermudez-Edo M, Gonzalez PC, Reyes FJO, Nousiainen T, Gutiérrez PJ, Moreno F, Muñoz O. On the application of scattering matrix measurements to detection and identification of major types of airborne aerosol particles: volcanic ash, desert dust and pollen. J Quant Spectrosc Radiat Transf 2021;271:107761.

[131] Martin JE, Hurd A. Scattering from fractals. J Appl Crystallogr 1987;20:61–78.

[132] Mason BJ, King S-J, Miles RE, Manfred KM, Rickards AM, Kim J, Reid JP, Orr-Ewing AJ. Comparison of the accuracy of aerosol refractive index measurements from single particle and ensemble techniques. J Phys Chem A 2012;116:8547–56.

[133] Mayer B, Kylling A. The libRadtran software package for radiative transfer calculations-description and examples of use. Atmospheric Chem Phys 2005;5: 1855–77.

[134] Mazzoni S, Potenza MA, Alaimo M, Veen S, Dielissen M, Leussink E, Dewandel J-L, Minster O, Kufner E, Wegdam G. SODI-COLLOID: a combination of static and dynamic light scattering on board the International Space Station. Rev Sci Instrum 2013;84:043704.

[135] Meng Z, Yang P, Kattawar GW, Bi L, Liou K, Laszlo I. Single-scattering properties of tri-axial ellipsoidal mineral dust aerosols: a database for application to radiative transfer calculations. J Aerosol Sci 2010;41:501–12.

[136] Mie G. Beiträge zur Optik trüber Medien, speziell kolloidaler Metallösungen. Ann Phys 1908;330:377–445.

[137] Min M, Rab C, Woitke P, Dominik C, Ménard F. Multiwavelength optical properties of compact dust aggregates in protoplanetary disks. Astron Astrophys 2016;585:A13.

[138] Miotello A, Robberto M, Potenza MA, Ricci L. Evidence of photoevaporation and spatial variation of grain sizes in the Orion 114-426 protoplanetary disk. Astrophys J 2012;757:78.

[139] Mishchenko MI, Hovenier JW, Travis LD. Light scattering by nonspherical particles: theory, measurements, and applications. Academic Press; 1999.

[140] Mishchenko MI, Liu L, Mackowski DW. T-matrix modeling of linear depolarization by morphologically complex soot and soot-containing aerosols. J Quant Spectrosc Radiat Transf 2013;123:135–44.

[141] Mishchenko MI, Travis LD. T-matrix computations of light scattering by large spheroidal particles. Opt Commun 1994;109:16–21.

[142] Mishchenko MI, Travis LD, Kahn RA, West RA. Modeling phase functions for dustlike tropospheric aerosols using a shape mixture of randomly oriented polydisperse spheroids. J Geophys Res Atmos 1997;102:16831–47.

[143] Mishchenko MI, Travis LD, Lacis AA. Scattering, absorption, and emission of light by small particles. Cambridge university press; 2002.

[144] Moosmüller H, Chakrabarty R, Arnott W. Aerosol light absorption and its measurement: a review. J Quant Spectrosc Radiat Transf 2009;110:844–78.

[145] Moteki N. Measuring the complex forward-scattering amplitude of single particles by self-reference interferometry: CAS-v1 protocol. Opt Express 2021;29: 20688–714.

[146] Moteki N. Capabilities and limitations of the single-particle extinction and scattering method for estimating the complex refractive index and size-distribution of spherical and non-spherical submicron particles. J Quant Spectrosc Radiat Transf 2020;243:106811.

[147] Moteki N. Discrete dipole approximation for black carbon-containing aerosols in arbitrary mixing state: a hybrid discretization scheme. J Quant Spectrosc Radiat Transf 2016;178:306–14. https://doi.org/10.1016/j.jqsrt.2016.01.025. Electromagnetic and light scattering by nonspherical particles XV: Celebrating 150 years of Maxwell's electromagnetics.

[148] Müller D, Weinzierl B, Petzold A, Kandler K, Ansmann A, Müller T, Tesche M, Freudenthaler V, Esselborn M, Heese B. Mineral dust observed with AERONET Sun photometer, Raman lidar, and in situ instruments during SAMUM 2006: shape-independent particle properties. J Geophys Res Atmos 2010;115.

[149] Muñoz O, Hovenier JW. Laboratory measurements of single light scattering by ensembles of randomly oriented small irregular particles in air. A review. J Quant Spectrosc Radiat Transf 2011;112:1646–57. https://doi.org/10.1016/j.jqsrt.2011.02.005. Electromagnetic and Light Scattering by Nonspherical Particles XII.

[150] Muñoz O, Volten H, Hovenier J, Veihelmann B, Van Der Zande W, Waters L, Rose WI. Scattering matrices of volcanic ash particles of Mount St. Helens, Redoubt, and Mount Spurr volcanoes. J Geophys Res Atmos 2004;109.

[151] Murr L, Garza K. Natural and anthropogenic environmental nanoparticulates: their microstructural characterization and respiratory health implications. Atmos Environ 2009;43:2683–92.

[152] Nakagawa M, Nakayama T, Sasago H, Ueda S, Venables DS, Matsumi Y. Design and characterization of a novel single-particle polar nephelometer. Aerosol Sci Technol 2016;50:392–404.

[153] Nakajima T, Campanelli M, Che H, Estellés V, Irie H, Kim S-W, Kim J, Liu D, Nishizawa T, Pandithurai G. An overview of and issues with sky radiometer technology and SKYNET. Atmospheric Meas Tech 2020;13:4195–218.

[154] Newton RG. Optical theorem and beyond. Am J Phys 1976;44:639–42.

[155] Onasch TB, Massoli P, Kebabian PL, Hills FB, Bacon FW, Freedman A. Single scattering albedo monitor for airborne particulates. Aerosol Sci Technol 2015;49: 267–79.

[156] Ortega-Arroyo J, Kukura P. Interferometric scattering microscopy (iSCAT): new frontiers in ultrafast and ultrasensitive optical microscopy. Phys Chem Chem Phys 2012;14:15625–36.

[157] Pagani L, Steinacker J, Bacmann A, Stutz A, Henning T. The ubiquity of micrometer-sized dust grains in the dense interstellar medium. Science 2010;329: 1622–4.

[158] Paganini E, Trespidi F, Ferri F. Instrument for long-path spectral extinction measurements in air: application to sizing of airborne particles. Appl Opt 2001; 40:4261–74.

[159] Pan Y-L, Aptowicz KB, Chang RK, Hart M, Eversole JD. Characterizing and monitoring respiratory aerosols by light scattering. Opt Lett 2003;28:589–91.

[160] Parola A, Piazza R, Degiorgio V. Optical extinction, refractive index, and multiple scattering for suspensions of interacting colloidal particles. J Chem Phys 2014; 141:124902.
[161] Pelssers E, Stuart MC, Fleer G. Single particle optical sizing (SPOS): I. Design of an improved SPOS instrument and application to stable dispersions. J Colloid Interface Sci 1990;137:350–61.
[162] Penttilä A, Zubko E, Lumme K, Muinonen K, Yurkin MA, Draine B, Rahola J, Hoekstra AG, Shkuratov Y. Comparison between discrete dipole implementations and exact techniques. J Quant Spectrosc Radiat Transf 2007;106:417–36.
[163] Pesic P. Estimating Avogadro's number from skylight and airlight. Eur J Phys 2004;26:183.
[164] Petrov D, Shkuratov Y, Videen G. Light scattering by arbitrary shaped particles with rough surfaces: sh-matrices approach. J Quant Spectrosc Radiat Transf 2012; 113:2406–18. https://doi.org/10.1016/j.jqsrt.2012.04.016. Electromagnetic and Light Scattering by non-spherical particles XIII.
[165] Pettit DR, Peterson TW. Coherent detection of scattered light from submicron aerosols. Aerosol Sci Technol 1982;2:351–68.
[166] Piedra P, Gobert C, Kalume A, Pan Y-L, Kocifaj M, Muinonen K, Penttilä A, Zubko E, Videen G. Where is the machine looking? Locating discriminative light-scattering features by class-activation mapping. J Quant Spectrosc Radiat Transf 2020;247:106936. https://doi.org/10.1016/j.jqsrt.2020.106936.
[167] Piedra P, Kalume A, Zubko E, Mackowski D, Pan Y-L, Videen G. Particle-shape classification using light scattering: an exercise in deep learning. J Quant Spectrosc Radiat Transf 2019;231:140–56. https://doi.org/10.1016/j.jqsrt.2019.04.013.
[168] Pierce PE, Maron SH. Prediction of minima and maxima in intensities of scattered light and of higher order Tyndall spectra. J Colloid Sci 1964;19:658–72.
[169] Pollack JB, Cuzzi JN. Scattering by nonspherical particles of size comparable to a wavelength: a new semi-empirical theory and its application to tropospheric aerosols. J Atmospheric Sci 1980;37:868–81.
[170] Potenza MA. The daylight sky and Avogadro's number. Eur J Phys 2015;36: 065040.
[171] Potenza MA, Albani S, Delmonte B, Villa S, Sanvito T, Paroli B, Pullia A, Baccolo G, Mahowald N, Maggi V. Shape and size constraints on dust optical properties from the Dome C ice core. Antarctica Sci Rep 2016;6:1–9.
[172] Potenza MA, Cremonesi L. On the quasi-universality of the forward light scattering lobe for micrometric objects. J Quant Spectrosc Radiat Transf 2022; 278:108028.
[173] Potenza MA, Krpetić Ž, Sanvito T, Cai Q, Monopoli M, De Araujo J, Cella C, Boselli L, Castagnola V, Milani P. Detecting the shape of anisotropic gold nanoparticles in dispersion with single particle extinction and scattering. Nanoscale 2017;9:2778–84.
[174] Potenza MA, Milani P. Free nanoparticle characterization by optical scattered field analysis: opportunities and perspectives. J Nanoparticle Res 2014;16:1–15.
[175] Potenza MA, Sabareesh K, Carpineti M, Alaimo M, Giglio M. How to measure the optical thickness of scattering particles from the phase delay of scattered waves: application to turbid samples. Phys Rev Lett 2010;105:193901.
[176] Potenza MA, Sanvito T, Alaimo M, Degiorgio V, Giglio M. Confocal zero-angle dynamic depolarized light scattering. Eur Phys J E 2010;31:69–72.
[177] Potenza MA, Sanvito T, Fazio G. Optical characterization of industrial slurries. KONA Powder Part J 2016. 2016016.
[178] Potenza MA, Sanvito T, Pullia A. Measuring the complex field scattered by single submicron particles. Aip Adv 2015;5:117222.
[179] Potenza MA, Sanvito T, Pullia A. Accurate sizing of ceria oxide nanoparticles in slurries by the analysis of the optical forward-scattered field. J Nanoparticle Res 2015;17:1–8.
[180] Potenza MA, Veen S, Schall P, Wegdam G. Nucleation of weakly attractive aggregates in microgravity. EPL Europhys Lett 2018;124:28002.
[181] Pratsinis SE. Aerosol-based technologies in nanoscale manufacturing: from functional materials to devices through core chemical engineering. AIChE J 2010; 56:3028–35.
[182] Purcell EM, Pennypacker CR. Scattering and absorption of light by nonspherical dielectric grains. Astrophys J 1973;186:705–14.
[183] Ravasio C, Cremonesi L, Artoni C, Delmonte B, Maggi V, Potenza MA. Optical characterization of mineral dust from the EAIIST project with digital holography. ACS Earth Space Chem 2021;5:2855–64.
[184] Rayleigh Lord. Investigations in capillarity. Phil Mag 1899;48:222.
[185] Rayleigh Lord. On the light from the sky, its polarization and colour. Phil Mag 1871;41:274.
[186] Raziman T, Somerville W, Martin OJ, Le Ru E. Accuracy of surface integral equation matrix elements in plasmonic calculations. JOSA B 2015;32:485–92.
[187] Revell LE, Kuma P, Le Ru EC, Somerville WRC, Gaw S. Direct radiative effects of airborne microplastics. Nature 2021;598:462–7. https://doi.org/10.1038/s41586-021-03864-x.
[188] Roco MC, Mirkin CA, Hersam MC. Nanotechnology research directions for societal needs in 2020: summary of international study. J Nanoparticle Res 2011.
[189] Romanov AV, Konokhova AI, Yastrebova ES, Gilev KV, Strokotov DI, Maltsev VP, Yurkin MA. Sensitive detection and estimation of particle non-sphericity from the complex Fourier spectrum of its light-scattering profile. J Quant Spectrosc Radiat Transf 2019;235:317–31.
[190] Romanov AV, Yurkin MA. Single-particle characterization by elastic light scattering. Laser Photonics Rev 2021;15:2000368. https://doi.org/10.1002/lpor.202000368.
[191] Royer A, De Angelis M, Petit J. A 30000 year record of physical and optical properties of microparticles from an East Antarctic ice core and implications for paleoclimate reconstruction models. Clim Change 1983;5:381–412.
[192] Saito M, Yang P, Ding J, Liu X. A comprehensive database of the optical properties of irregular aerosol particles for radiative transfer simulations. J Atmospheric Sci 2021;78:2089–111.
[193] Sanford TJ, Murphy DM, Thomson* DS, Fox RW. Albedo measurements and optical sizing of single aerosol particles. Aerosol Sci Technol 2008;42:958–69.
[194] Sanvito T, Bigini P, Cavanna MV, Fiordaliso F, Violatto MB, Talamini L, Salmona M, Milani P, Potenza MA. Single particle extinction and scattering optical method unveils in real time the influence of the blood components on polymeric nanoparticles. Nanomed Nanotechnol Biol Med 2017;13:2597–603.
[195] Scanza R, Mahowald N, Ghan S, Zender C, Kok J, Liu X, Zhang Y, Albani S. Modeling dust as component minerals in the Community Atmosphere Model: development of framework and impact on radiative forcing. Atmos Chem Phys 2015;15:537–61.
[196] Schebarchov D, Le Ru E, Grand J, Auguié B. Mind the gap: testing the Rayleigh hypothesis in T-matrix calculations with adjacent spheroids. Opt Express 2019;27: 35750–60.
[197] Shen Y, Draine B, Johnson ET. Modeling porous dust grains with ballistic aggregates. I. Geometry and optical properties. Astrophys J 2008;689:260.
[198] Simonsen MF, Cremonesi L, Baccolo G, Bosch S, Delmonte B, Erhardt T, Kjær HA, Potenza MA, Svensson A, Vallelonga P. Particle shape accounts for instrumental discrepancy in ice core dust size distributions. Clim Past 2018;14:601–8.
[199] Smoluchowski M. Molekular-kinetische Theorie der Opaleszenz von Gasen im kritischen Zustande, sowie einiger verwandter Erscheinungen. Ann Phys 1908; 330:205–26.
[200] Somerville W, Auguié B, Le Ru E. SMARTIES: user-friendly codes for fast and accurate calculations of light scattering by spheroids. J Quant Spectrosc Radiat Transf 2016;174:39–55.
[201] Somerville W, Auguié B, Le Ru E. Accurate and convergent T-matrix calculations of light scattering by spheroids. J Quant Spectrosc Radiat Transf 2015;160:29–35.
[202] Sorensen CM. Q-space analysis of scattering by particles: a review. J Quant Spectrosc Radiat Transf 2013;131:3–12.
[203] Sorensen CM. Light scattering by fractal aggregates: a review. Aerosol Sci Technol 2001;35:648–87.
[204] Sorensen CM, Fischbach D. Patterns in Mie scattering. Opt Commun 2000;173: 145–53.
[205] Sorensen CM, Roberts GC. The prefactor of fractal aggregates. J Colloid Interface Sci 1997;186:447–52.
[206] Sorensen CM, Shi D. Patterns in the ripple structure of Mie scattering. JOSA A 2002;19:122–5.
[207] Sorensen CM, Shi D. Guinier analysis for homogeneous dielectric spheres of arbitrary size. Opt Commun 2000;178:31–6.
[208] Sorensen CM, Yon J, Liu F, Maughan J, Heinson WR, Berg MJ. Light scattering and absorption by fractal aggregates including soot. J Quant Spectrosc Radiat Transf 2018;217:459–73.
[209] Stegmann PG, Johnson B, Moradi I, Karpowicz B, McCarty W. A deep learning approach to fast radiative transfer. J Quant Spectrosc Radiat Transf 2022;280: 108088. https://doi.org/10.1016/j.jqsrt.2022.108088.
[210] Stocker T. Climate change 2013: the physical science basis: working group I contribution to the fifth assessment report of the intergovernmental panel on climate change. Cambridge university press; 2014.
[211] Stognienko R, Henning T, Ossenkopf V. Optical properties of coagulated particles. Astron Astrophys 1995;296:797.
[212] Sun B, Yang P, Kattawar GW, Zhang X. Physical-geometric optics method for large size faceted particles. Opt Express 2017;25:24044–60.
[213] Taflove A, Hagness S. Computational electrodynamics: the finite-difference time-domain method. Boston, MA: Artech House; 2000.
[214] Taubenblatt MA, Batchelder JS. Measurement of the size and refractive index of a small particle using the complex forward-scattered electromagnetic field. Appl Opt 1991;30:4972–9.
[215] Taylor RW, Sandoghdar V. Interferometric scattering microscopy: seeing single nanoparticles and molecules via Rayleigh scattering. Nano Lett 2019;19:4827–35.
[216] Tinke A, Carnicer A, Govoreanu R, Scheltjens G, Lauwerysen L, Mertens N, Vanhoutte K, Brewster M. Particle shape and orientation in laser diffraction and static image analysis size distribution analysis of micrometer sized rectangular particles. Powder Technol 2008;186:154–67.
[217] Twomey S. On the numerical solution of Fredholm integral equations of the first kind by the inversion of the linear system produced by quadrature. J ACM JACM 1963;10:97–101.
[218] Tyndall J. On the blue colour of the sky and the light of the sky. Phil Mag 1869; 37:384–94.
[219] van de Hulst HC. Light scattering by small particles (Courier corporation). New York, NY, USA: Dover Publications, Inc.; 1957.
[220] Veen SJ, Antoniuk O, Weber B, Potenza MA, Mazzoni S, Schall P, Wegdam GH. Colloidal aggregation in microgravity by critical Casimir forces. Phys Rev Lett 2012;109:248302.
[221] Videen G, Zubko E, Sun W, Shkuratov Y, Yuffa A. Mixing rules and morphology dependence of the scatterer. J Quant Spectrosc Radiat Transf 2015;150:68–75. https://doi.org/10.1016/j.jqsrt.2014.07.022. Topical issue on optical particle characterization and remote sensing of the atmosphere: Part I.
[222] Villa S, Sanvito T, Paroli B, Pullia A, Delmonte B, Potenza MA. Measuring shape and size of micrometric particles from the analysis of the forward scattered field. J Appl Phys 2016;119:224901.
[223] Volten H, Jalava J-P, Lumme K, Haan JFde, Vassen W, Hovenier JW. Laboratory measurements and T-matrix calculations of the scattering matrix of rutile particles in water. Appl Opt 1999;38:5232–40. https://doi.org/10.1364/AO.38.005232.

[224] Voshchinnikov N, Il'in V, Henning T, Michel B, Farafonov V. Extinction and polarization of radiation by absorbing spheroids: shape/size effects and benchmark results. J Quant Spectrosc Radiat Transf 2000;65:877–93.
[225] Walker JS, Carruthers AE, Orr-Ewing AJ, Reid JP. Measurements of light extinction by single aerosol particles. J Phys Chem Lett 2013;4:1748–52. https://doi.org/10.1021/jz4008068.
[226] Walser A, Sauer D, Spanu A, Gasteiger J, Weinzierl B. On the parametrization of optical particle counter response including instrument-induced broadening of size spectra and a self-consistent evaluation of calibration measurements. Atmospheric Meas Tech 2017;10:4341–61.
[227] Walters S, Zallie J, Seymour G, Pan Y-L, Videen G, Aptowicz KB. Characterizing the size and absorption of single nonspherical aerosol particles from angularly-resolved elastic light scattering. J Quant Spectrosc Radiat Transf 2019;224:439–44.
[228] Weitz D, Oliveria M. Fractal structures formed by kinetic aggregation of aqueous gold colloids. Phys Rev Lett 1984;52:1433.
[229] Wells, D., Nicoli, D.F., 1998. Single-particle optical sensor with improved sensitivity and dynamic size range.
[230] Wheeler JA, Feynman RP. Interaction with the absorber as the mechanism of radiation. Rev Mod Phys 1945;17:157.
[231] Whitby KT, Vomela RA. Response of single particle optical counters to nonideal particles. Environ Sci Technol 1967;1:801–14.
[232] Winkler A, Fumagalli F, Cella C, Gilliland D, Tremolada P, Valsesia A. Detection and formation mechanisms of secondary nanoplastic released from drinking water bottles. Water Res. 2022;222:118848. https://doi.org/10.1016/j.watres.2022.118848.
[233] Wriedt T. Light scattering theories and computer codes. J Quant Spectrosc Radiat Transf 2009;110:833–43.
[234] Wu L, Hasekamp O, van Diedenhoven B, Cairns B, Yorks JE, Chowdhary J. Passive remote sensing of aerosol layer height using near-UV multiangle polarization measurements. Geophys Res Lett 2016;43:8783–90.
[235] Ysard N, Jones A, Demyk K, Boutéraon T, Koehler M. The optical properties of dust: the effects of composition, size, and structure. Astron Astrophys 2018;617:A124.
[236] Yurkin MA, Hoekstra AG. The discrete-dipole-approximation code ADDA: capabilities and known limitations. J Quant Spectrosc Radiat Transf 2011;112:2234–47.
[237] Zhang R, Khalizov A, Wang L, Hu M, Xu W. Nucleation and growth of nanoparticles in the atmosphere. Chem Rev 2012;112:1957–2011. https://doi.org/10.1021/cr2001756.
[238] Zhong Z, Bai H, Shan M, Zhang Y, Guo L. Fast phase retrieval in slightly off-axis digital holography. Opt Lasers Eng 2017;97:9–18.
[239] Zimm BH. The scattering of light and the radial distribution function of high polymer solutions. J Chem Phys 1948;16:1093–9.
[240] Zimm BH. Apparatus and methods for measurement and interpretation of the angular variation of light scattering; preliminary results on polystyrene solutions. J Chem Phys 1948;16:1099–116.